GATED WAVEFRONT SENSING

ONG CHI WEI

A project report submitted in partial fulfilment of the

requirements for the award of the degree of

Bachelor (Hons.) of Biomedical Engineering

Faculty of Engineering and Science

Universiti Tunku Abdul Rahman

April 2011

DECLARATION

I hereby declare that this project report is based on my original work except for citations and quotations which have been duly acknowledged. I also declare that it has not been previously and concurrently submitted for any other degree or award at UTAR or other institutions.

Signature : _____

Name   : _____

ID No.   : _____

Date   : _____

APPROVAL FOR SUBMISSION

I certify that this project report entitled **"GATED WAVEFRONT SENSING"** was prepared by **ONG CHI WEI** has met the required standard for submission in partial fulfilment of the requirements for the award of Bachelor of Engineering (Hons.) Biomedical Engineering at Universiti Tunku Abdul Rahman.

Approved by,

Signature : _____

Supervisor : Dr.Tan Ching Seong

Date   : _____

Specially dedicated to

my beloved mother and father

ACKNOWLEDGEMENTS

This dissertation would not have been possible without the guidance and the help of several individuals who in one way or another contributed and extended their valuable assistance in the preparation and completion of this study.

First and foremost, my utmost gratitude to Dr. Tan Ching Seong, my final year project supervisor whose sincerity and encouragement I will never forget. Dr. Tan Ching Seong has been my inspiration as I hurdle all the obstacles in the completion this research work.

I am deeply indebted to Dr.Wang Xin, had kind concern and consideration regarding my final year project progress.

The project will not possible to finish without Mr Kenneth Wong Fatt Kong's help in the microprocessor lab. He has shared valuable insights in the relevance of the study in the technology sector and offered help in fabrication of holes array.

I would like to show my gratitude to all the staff in UTAR for the use of facilities in the mechanical workshop.

Lastly, I offer my regards and blessings to all of those who supported me in any respect during the completion of the project.

GATED WAVEFRONT SENSING

ABSTRACT

With the breakthrough of manufacturing technology, large scale wafer can be fabricated with high throughput. However, inspection technology still cannot meet the industrial requirements. Visual inspection technique still widely applied in semi conductor industry for many years although it is slow and tedious. Currently laser surface scanning Inspection systems (SSIS) have been widely used to automate wafer particle inspection system but SSIS are not capable to identify and classify a variety of crystalline defects such as dislocations, slip lines, stacking faults, voids, and mounds in the subsurface of wafer. CT scanning and other imaging system can achieve high accuracy but it is high cost and low speed. There is often a trade off between the quality of wafer and inspection technology. In this project a novel technique has been proposed to perform multi-layer inspection to reduce the wafer surface and subsurface defect.

In this project conceptual optical design system has been studied and applied in the optical laboratory. An environment and device which is similar to wafer in real environment has been constructed to demonstrate our conceptual design. Aperture array has been made to simulate the result which will allow us to apply image processing technique for centroiding. Conventional technique for centroiding and new developed centroiding algorithm has both been compared and contrast in the project.

At the mean time, zonal method reconstruction algorithm to reconstruct the wafer surface profile has been developed. It is able to achieve root mean square error lower than 1%. Both zonal and modal reconstruction has been applied in the project for phase reconstruction of wavefront. The variance of result of both methods is very low and it shows the validity for our zonal method reconstruction algorithm.

Based on the surface profile, a novel multilayer inspection numerical model has been developed to allow user to investigate the subsurface defect. A simulation has been done based on the numerical model. A friendly graphical user-interface has been developed based on Matlab environment for communication between researchers and end-user. A standard operating procedure for optical laboratory has been constructed throughout the project in optical lab for education usage.

TABLE OF CONTENTS

LIST OF TABLES

LIST OF FIGURES

LIST OF SYMBOLS / ABBREVIATIONS

θ_i	Angle of incidence (incoming)
θ_r	Angle of reflection (outgoing)
θ_t	Angle of transmission
n	Index of refraction
d	Layer thickness [mm]
δ	Phase
$\vec{\gamma}$	Arbitrary plane wave
$\overrightarrow{\gamma_n^x}$	x-component of arbitrary plane wave
$\overrightarrow{\gamma_n^y}$	y-component of arbitrary plane wave
ϕ	Relative angle
$\overrightarrow{\zeta_n^x}$(zeta)	Reflected wave for x component plane wave
$\overrightarrow{\zeta_n^y}$	Reflected wave for y component plane wave
$\overrightarrow{\gamma_{n+1}^x}$	Transmission wave for x component plane wave
$\overrightarrow{\gamma_{n+1}^y}$	Transmission wave for y component plane wave
$\overrightarrow{\zeta_{n+1}^x}$	For symmetry purpose
$\overrightarrow{\zeta_{n+1}^y}$	For symmetry purpose
α_i	Incident angle for the x component plane wave
β_i	Incident angle for the y component plane wave
α_r	reflected angle for the x component plane wave
β_r	Reflected angle for the y component plane wave
α_t	Transmitted angle for the x component plane wave
β_t	Transmitted angle for the y component plane wave

LIST OF APPENDICES

Chapter 1

Introduction

1.1 Background

Following Moore's law, component density and performance of integrated circuits doubles every year which was then revised to doubling every two years. The complexity of integrated circuits can only be achieved by very fast, smooth, and defect-free wafer surfaces. Recently manufactures of silicon wafers have been striving for achieve a flat, smooth, and defect free surface to maintain a good quality integrated circuit. There is why our idea for this final year project comes in. Our goal is to **design an optical system which is able to do wafer surface inspection by gated wavefront sensing.**

Generally, a smooth wafer can be produced by carefully polishing the surface and the quality of surface smoothness can reach a certain level that is significantly better than most optical surfaces. Unfortunately, not all defects are on the surface. Many defects are caused by the surface- finishing process and reside just below the surface in damaged layer. These subsurface defects affect the quality of wafer surface. **Our second goal is perform multilayer wafer inspection by gated wavefront sensing through the optical system.**

Defect detection can be performed by directly comparing the two complex wavefronts taken from corresponding fields of view from adjacent die on the wafer. To isolate which field of view a detected defect is in, two comparisons are made for each field of view, and the defect is ascribed to that field only if it appears in both difference images. We use Shart-Hartmann sensor design concept to help us to

capture the wavefront. A key step in processing the wavefront sensing data is to centroid the spots captured by a detector array. These centroids are used to estimate the local slopes which are then combined to give the overall wavefront reconstruction.**We are going to develop a new algorithm to perform centroiding for estimating wavefront slope from wavefront data. The wavefront slope is going to be used in wavefront reconstruction.**

A series of computations are required to reconstruct the complete wavefront returning from the wafer surface from the off-axis hologram and its interference fringes in modal approach. The reconstructed complex wavefront is usually visualized as two separate images, one representing the amplitude of the complex wave and the other representing the phase. The phase image can be corrected using the reconstructed image of a flat surface in the object arm. The wavefront reconstruction technique corrects for any curvature present in the object wave that is not caused by the object itself. It does improve the visual appearance of the phase images because it removes distracting phase wraps (where the phase jumps suddenly between –p radians to +p radians) from the image. (Schulze, Hunt, Voelkl, Hickson, & Usry, 2003) Fourier transform is one of the spotlights in modal approach research and there is a lot of computational methods explain it. **We are going to develop a new algorithm based on the zonal method to accomplish the wavefront reconstruction and verify it with Zernike reconstruction.**

To perform wavefront inspection, our motivation comes from the gated image capturing. It followed the basic principles of radar and sonar technologies that have been used for many decades. A laser illuminator generates short pulses that reflect from the object return to a camera with electronically controlled (gated) shutter of very short opening time. By controlling the pulse width and the shutter opening time, it is possible to capture an image that contains only objects within a predefined distance from the camera. (Sluzek & Tan, 2004) Similarly, we can use it to help us to capture the wavefront which comes from different layer of wafer, and perform wavefront reconstruction and detect the defect.

1.2 Aim and Objectives:

The aim of this final year project is using low cost device to build an optical system and develop new algorithm to perform wafer inspection so that both can bring a solution for achieving a smooth and flat wafer.

The work scopes are:

1. Develop multi layer surface profiling theory for gated wavefront sensing

2. Develop a new algorithm to perform centroiding finding

3. Design an optical system to do wavefront sensing

4. Develop algorithm to accomplish the wavefront phase reconstruction using zonal/modal approach

1.3 Project Methodology

In this project, we design an optical system to perform wafer surface profiling using the dark room accessories following with the working flowchart as shown below.

Proposed working flow chart:
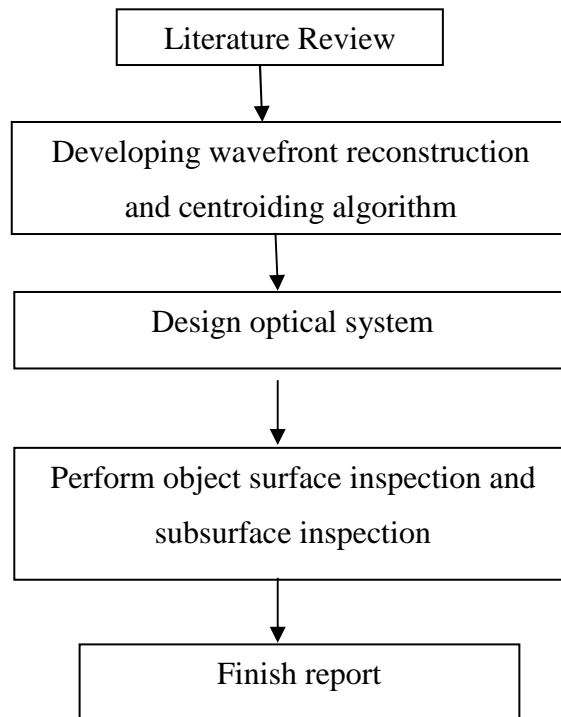
Figure 1.1 Working Flow Chart

To complete the project, we buy the items as listed below to construct the optical system for wavefront sensing.

Table 1.1 Purchasing Item

No.	Items
1	5mm Uncoated Right Angle Prism
2	650nm Laser Line Polarizing Beamsplitter Cube
3	Uncoated BK7 Plano-Convex Lenses(F/L=15mm))
4	2 Dia0.5-inch BK7 Plano-Concave Lenses AR@650-1050nm(F/L=15mm

Gantt chart for project progress outline

Table 1.2 Gantt Chart

	2010							2011				
	YEAR 4											
	SEMESTER 1				BREAK			SEMESTER 2				
	JUNE	JULY	AUGUST	SEPTEMBER	OCTOBER	NOVEMBER	DECEMBER	JANUARY	FEBRUARY	MARCH	APRIL	MAY
Literature Review												
Wafer Inspection	▓	▓	▓	▓								
Wavefront measurement	▓	▓	▓	▓								
Wavefront Reconstruction	▓	▓	▓	▓								
Multilayer wavefront Inspection					▓	▓	▓	▓				
Experiment Progress												
Algorithm development			▓	▓	▓	▓	▓					
Optical system			▓	▓	▓	▓	▓	▓	▓	▓		
Report & Presentation												
Progress Report				▓								
Final Report												▓
Presentation				▓								

1.4 Thesis outline

This report is divided into five sections to describe to the readers in detail of the whole project. It is written following ILMRDC (Introduction, literature review, methodology, results, discussion and conclusion) structure. The first section is the introduction of the background of the project. It identifies a few issues currently faced in the current wafer inspection technology and list out the aims and the objectives of the project.

The second section is the literature review done on the journals found related to the project. In this section, current research on the wafer inspection technology is listed out. Gated wavefront sensing concept is being introduced through some review. Centroiding technique and wavefront phase reconstruction developed in the past has been studied in this part. Multilayer inspection theory is also briefly been given a review focusing on the current trend.

The third section introduces the methodology in details of the decided method to perform the experiment. An optical system design is shown in this part for demonstrate the capability to doing wavefront sensing use our current optical laboratory. A Gantt chart and cost is also listed out shows that the strategic plan and cost control for this project.

The following section focus on the results and discussion. I divide this section into two chapters due of intensive data and algorithm applied. Chapter 4 we discuss about the reconstruction of gated wavefront sensing. This chapter consists of the method for zonal reconstruction and centroiding theory and how I build numerical model of multilayer. Different theory and computer simulation result has been shown and discuss in this chapter. Chapter 5 turns the theory and simulation into the real working environment. Centroiding results are listed out and both zonal and modal reconstruction technique is applied to verify the algorithm is valid and sufficient to perform the intended purpose.The last section is the conclusion and recommendation. For this section, a summary of the project is given. The future development and value of the project is being discussed.

Chapter 2

Literature Review

2.1 Development of wafer inspection technology

For the past few years, the international technology roadmap for semiconductors (ITRS) has highlighted the increasing need for technologies that address key defect detection and characterization requirements. (International Technology Roadmap for Semiconductors, 2000) Good quality chips can only be achieved once we manage to get flat and smooth wafer. That is one of reason why wafer inspection in semiconductor assembly manufacturing has become increasingly important over the past several years as a means of quickly understanding and controlling contamination sources and process faults, which impact the product yield.

Automation technologies in defect detection and review are being developed by universities, laboratories, industry, and semiconductor equipment suppliers. Several techniques were adopted, such as automatic defect classification (ADC) on the sub-die or defect level and spatial signature analysis (SSA) on the whole-wafer level. (Shankar & Zhong, 2004)

Different defect detection technique has their pros and cons. (Shankar & Zhong, 2004) For example, automatic defect classification (ADC) on the sub-die or defect level and spatial signature analysis (SSA) on the whole-wafer level. One of the few commercially available ADC systems extracts numerous spatial and textural features from the defect region, and applies a set of user defined fuzzy predicates for

defining the defect classes. The main draw back of ADC is the time consumption and also there is no reference pattern for the whole process, i.e., it considers neighboring die as reference for the die under inspection. On the other hand, SSA has no relation with the defect data generated by local anomalies caused during wafer mounting, dicing, imbedded particle contamination, etc. (Shankar & Zhong, 2004)

Automated techniques that have been developed to perform wafer inspection task through the image processing techniques Several promising well-known techniques such as digital holography (Dai, Hunt, & Schulze, 2003), digital shearography (Udupa, Ngoi, Goh, & Yusoff, 2004)and semiconductor neural networks system have been developed and reported by several research groups. (Kameyama & Kosugi, 2002) Rule-based inspections of semiconductor wafer surface have been reported (Shankar & Zhong, 2003)

Defect detection usually is performed by directly comparing the two complex wavefronts taken from corresponding fields of view from adjacent die on the wafer. Difference images can be computed as either amplitude or phase or as a composite difference. In order to compare two images from different die, the pixel values must be aligned in the x- and y-directions (spatial registration) and matched in terms of their overall intensity and phase offset (normalization). (Shankar & Zhong, 2004)Spatial registration of the complex images can be performed via an automatic registration algorithm previously. (Dai, Hunt, & Schulze, 2003)

Laser-based optical wafer surface profiling techniques, using laser beam reflection from the blanket wafer surface, have been widely used in the semiconductor industry for rough inspection of wafer flatness, wafer bow and process induced stress after film deposition. However the application was limited to rough surface profile measurements of blanket wafers only. Due to the optical sensing, wafer holding and wafer rotation/translation mechanisms used in the system, fine measurement in the submicron range wafer inspection are not possible using conventional wafer flatness and profile inspection systems. (Woo, Ueda, Ishigaki, & Kang, 2010)

The chronological technology improvement in the past ten years as listed below.Note that only first author are listed out.

Table 2.1 Wafer Inspection Technology Review

Year	Author	Description
1999	Stan Stokowski	Wafer Inspection Technology Challenges for ULSI Manufacturing has been introduced. Extensions of these technologies to meet the requirements of manufacturing integrated circuits with smaller structures on larger wafers are discussed.(Stokowski & Vaez-iravani, 1999)
2000	Thomas A. Germer	A polarized Light Scattering Techniques for Surface Wafer Inspection has been discussed. Laser inpection defect technique on surface of wafer condition has been discussed. (Germer, 2000)
2000	Koji Nakamae	An question has been proposed, that an inline wafer inspection strategy, high sensitivity & high cost inspection machine or low sensitivity & low cost inspection machine should be used in an inline wafer inspection strategy? Simulated results show that setting an adequate wafer rejection condition and selecting a proper sampling plan obtain the minimum cost per chip regardless of the kind of inspection machine.(Nakamae, Yamaji, & Fujioka, 2000)
2004	N.G. Shankar	Defect detection on semiconductor wafer surfaces has been discussed and review in the paper. The author developed a template-based vision system but not for the 100% wafer surface profiling and inspection. The experimental results have proven to be good, statistically for the projected mean square error for several species of wafer die sizes.(Shankar & Zhong, 2005)
2006	Akira Hamamatsu	A common method of wafer inspection is the die to die comparison method. Authors developed a statistical threshold method for semiconductor inspection in which the brightness variation is adapted based on the background is developed.(Hamamatsu et al., 2006)

2.2 Review of Wavefront Sensing

The principle of wavefront sensing can be illustrated as below (Sluzek & Tan, 2004)
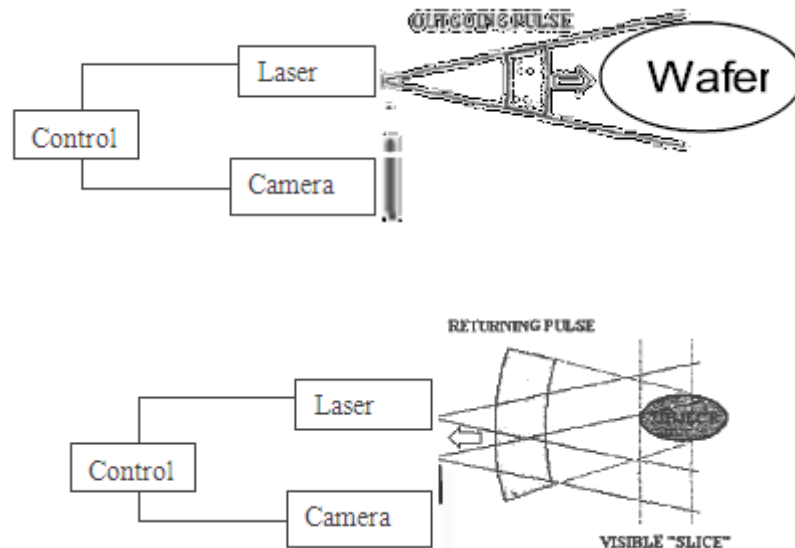
Figure 2.1 Principle of Gated Wavefront Sensing (Sluzek & Tan, 2004)

By controlling the pulse width and the shutter opening time, it is possible to capture an image that contains only objects within a predefined distance from the camera. (Sluzek & Tan, 2004) The wavefront reflected from the wafer and shutter opening time can be controlled, so the shutter can capture the wavefront from the surface and subsurface. By compare them with a reference wavefront refrected from a defect-free wafer, we can know whether any defect on the surface.

In this project, we simply change a pulse into wavefront. We need to understand what wavefront is before we measure it. As described in shadow casting phenomena and the pinhole camera, light travelled in straight line. The pinhole camera is useful to define what is meant by a "ray of light". Consider a point source of light, emitting rays in all direction. Next, we consider the ensemble of rays having a certain optical path length (OPL) (Tyson, 2000)

$$U = U_O \sin k \, (x\text{-}ct)$$
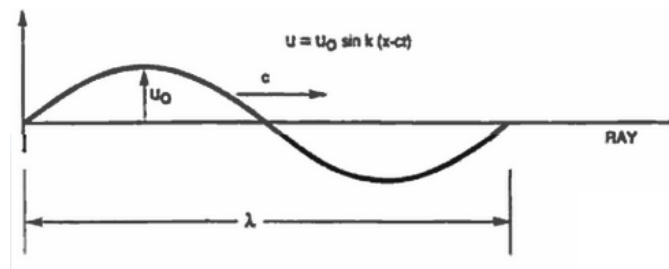
Figure 2.2 Example of Basic Monochromatic Wave Structure Propagating Along a Ray. (Tyson, 2000)

The OPL is a radius in this case and the ray tips lie on the surface of a sphere (centered on the point source). This surface is a basis example of what is meant by a wavefront. (Note that rays and their associated wavefront are always orthogonal to one another.) In general term, a surface over which the phase of a wave is constant is called a wavefront. (Tyson, 2000)

In many instances of interest, the spherical wavefront and flat wavefront are ideal construction against which other wavefronts will be compared, in this project, we call them reference wavefronts.

The basic component we need to measure the wafer wavefront is a Shack Hartmann sensor. The wafer defect can detected through a system like Columbus System. (Raymond, Neal, & Topa, 2002)
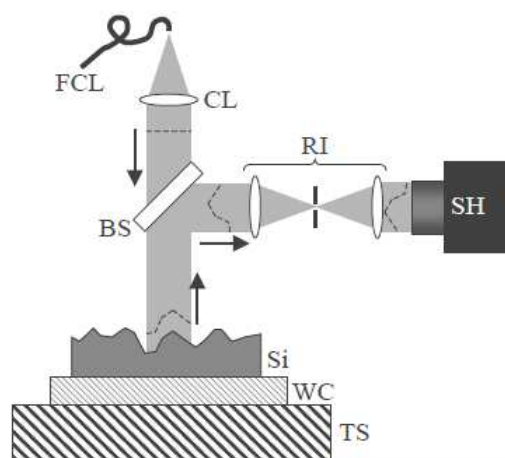
Figure 2.3 Columbus System (Raymond, Neal, & Topa, 2002)

In the Columbus system, A fiber coupled 635 nm laser diode light source is collimated and directed onto the wafer surface. The wafer is mounted on a wafer chuck attached to a two-axis translation stage capable of positioning the wafer so that the entire surface can be analyzed one patch at a time. The phase of the reflected light is imprinted with the height variations on the wafer surface. The reflected light is imaged, using a simple 1:1 relay telescope, onto a Shack-Hartmann wavefront sensor for analysis of the phase, and thus the wafer surface. This kind of system has recently proven to be very effective at measurement of wavefront. (Raymond, Neal, & Topa, 2002)

The essential components in Shack –Hartmann sensor are a light source, an array of lenslets array and a camera or something which is able recording the pattern of images formed by the lenslets in the array (Tyson, 2000). The figure below is a schematic diagram of a Shack-Hartmann sensor. It can be illustrated as next page.
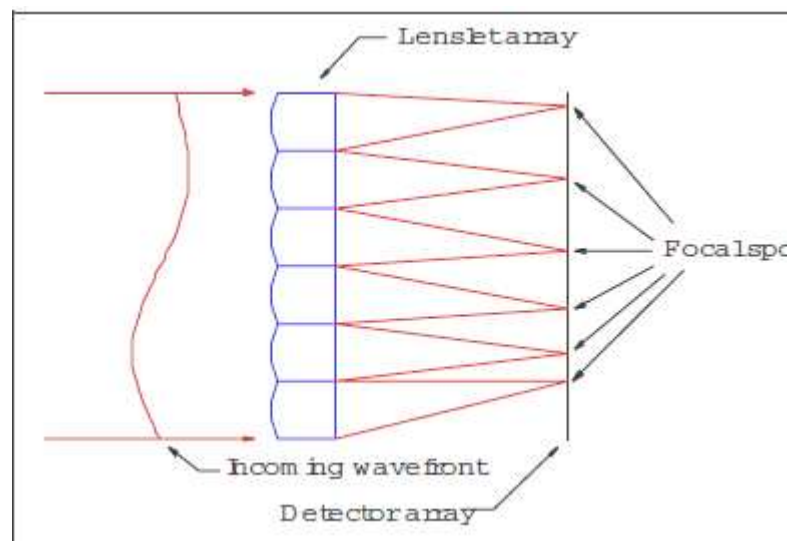
Figure 2.4 Schematic Diagram of a Shack-Hartmann Sensor
(Neal, Copland, & Neal, 2002)

In our project, we are going to build our own hole array to replace the lenslets array due to cost problem. Once we manage to get the wavefront data, we can perform analysis process. There are three steps in the analysis process: determination of the

spot positions (centroiding), conversion to wavefront slopes, and wavefront reconstruction.

The recent review of using Shack-Hartmann sensor for wavefront reconstruction has been listed in table 2.2.

Table 2.2 Recent Review of Shark-Hartmann Sensor

| Year	Author (s)	Description
2003	Daniel R. Neal	A Shack -Hartmann wavefront sensor (SHWFS) has been used for the measurement of highly aberrated large optics. It is used to test large (300 mm) fused silica wafers in double pass transmission with a megapixel camera equipped with 100x100 lenslets. It is expected to achieve several hundred waves of dynamic range with better than $\lambda/20$ accuracy.(Neal, Pulaski, Raymond, & Neal, 2003)
2004	Daniel R. Neal	Historical background of the development of the Shack-Hartmann wavefront sensor has been reviewed. Different application of Shack-Hartmann sensor in commercial application like semi-conductor industry.(Neal, 2004)
2004	Brent L. Ellerbroek	A Shack-Hartmann wave front sensor with 8 subapertures has been used on the astronomy area. Performance of closed loop adaptive optics system can be maximized using multiple control bandwidths.(Ellerbroek, 1994)

2.3 Spot array centroiding technique

For centroiding a pixilated sensor like CCD detector, the location of the focal spots is determined from the light distribution on the detector array. For a sampled irradiance distribution with measured pixel intensities E_{ij}, the spot positions $x_{c,\,k}$ and $y_{c,k}$ are commonly determined by the first moments: (Neal, Copland, & Neal, 2002)

$$x_{c,k} = \frac{\sum_{i,j \in AOI_k} x_{i,j} I_{i,j}}{\sum_{i,j \in AOI_k} I_{i,j}} \tag{2.1}$$

$$y_{c,k} = \frac{\sum_{i,j \in AOI_k} y_{i,j} I_{i,j}}{\sum_{i,j \in AOI_k} I_{i,j}} \tag{2.2}$$

where the index k is over the lenslet number with center position $(x_l, y_l)_k$ and the summation is taken over the pixels assigned to the lenslet k, in Area-of-Interest $AOIk$.11 There are a number of variations to this, including thresholding or image deconvolution, that affect the accuracy of this determination. All of these methods result in the estimation of the position of the focal spots across the array.

The wavefront slope distribution is determined by comparison of the measured centroids to a reference wavefront. The reference can be determined only from the positions of the lenslet centers, but more commonly it is recorded using a reference wavefront measured with the wavefront sensor system. For a set of measured centroids $(x_c, y_c)_k$ and reference centroids $(x_r, y_r)_k$, the wavefront slope distribution is:

$$\begin{pmatrix} \langle \partial w / \partial x \rangle \\ \langle \partial w / \partial y \rangle \end{pmatrix} = \begin{pmatrix} \beta_x \\ \beta_y \end{pmatrix}_k = \frac{1}{L_H} \begin{pmatrix} x_c - x_r \\ y_c - y_r \end{pmatrix}_k \tag{2.3}$$

where L_H, the distance between the lenslet array and detector, is normally set to the lenslet focal length, f.

Centroiding technique has been widely study for the past few years. Conventional method [(Yin, Li, Zhao, & Fang, 2009) (A.Vyas, M. B. Roopashree, & B.R.Prasad., 2010)] a high intensity spot has been chosen to create a pattern or generate a threshold so image processing technique can be applied to recognize the centre of the spot. J. Ares and J. Arines have presented a full analytical description of the interaction between centroiding and thresholding applied over an intensity distribution corrupted by additive Gaussian noise. The analytical description of J.Ares and J.Arines has been applied as golden standard in the Gaussian noise adding processing. However, it starts from optic views. Adaptive thresholding for centroiding has been applied these few years but the accuracy and stability of results still not yet has analytical description and consistency of the results still in a doubt.

2.4 Wavefront reconstruction

Now we can perform the wavefront reconstruction using the wavefront slope. Wavefront reconstruction technique corrects for any curvature present in the wafer wave that is not caused by the wafer itself. Wavefront reconstruction can be constructed through zonal approach and modal approach. In general, wavefront reconstruction can be categorized into two approaches, zonal and modal. In the zonal concept, the wavefront in a certain sub-aperture is fitted by means of phase directional derivative measurements. In the modal concept, wavefront is decomposed into a series of orthogonal polynomials, and the coefficients of the polynomials are estimated using the phase derivative measurements. Both methods use least square estimation. (Dai G. M., 2008)

For our project, we use a zonal method proposed by Southwell (Southwell, 1980) to help us to solve wavefront reconstruction problem.

Configuration A   Configuration B   Configuration C
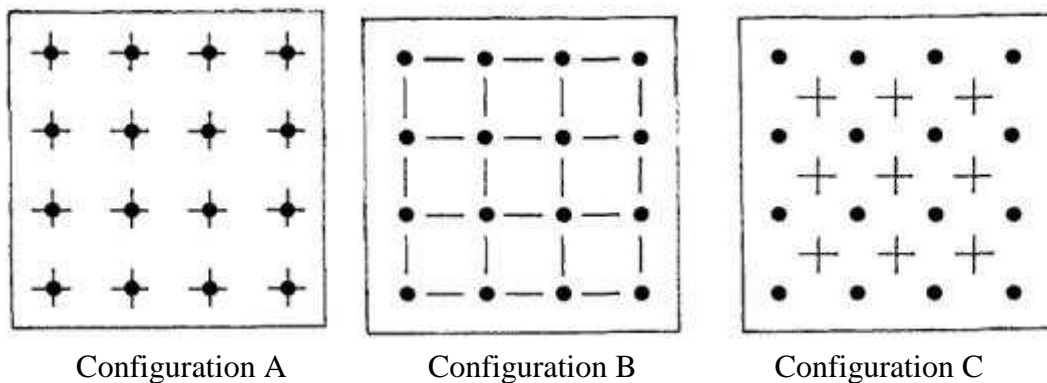
Figure 2.5 Slope Measurement Sampling Geometry and Wavefront Mesh Points

The horizontal dashes indicate positions of x-slope sampling. The vertical dashes are the y-slope sampling positions. The dots are the estimated phase points. Configuration B has been considered previously by Hudgin and configuration C by Fried. Configuration A is considered by W.H.Southwell also will be used in our project.

The phase can be achieved through the following formula proposed by W.H.Southwell. (Southwell, 1980)

$$\frac{\left(S^x_{i+1,j}+S^x_{ij}\right)}{2} = \frac{(\phi_{i+1,j}-\phi_{ij})}{h} \quad \begin{array}{l} i = 1, N-1 \\ j = 1, N \end{array} \tag{2.4}$$

$$\frac{\left(S^y_{i+1,j}+S^y_{ij}\right)}{2} = \frac{(\phi_{i+1,j}-\phi_{ij})}{h} \quad \begin{array}{l} i = 1, N \\ j = 1, N-1 \end{array} \tag{2.5}$$

where   S= Slope data

Ø= Phase data,

h=D/N

D = width of the aperture

N=number of hole.

The equation can be simplified to below

$$S = A\phi \tag{2.6}$$

where S= Slope data

A= Constant

ϕ= Phase data

The above equation shows there is liner relationship between slope data and wavefront phase.

W.H.Southwell proposed matrix iterative solution, which can use sparse matrix to help us to solve linear equation, which is further evaluated in my algorithm prototype. (Southwell, 1980)

$$g_{jk}\phi_{jk} - [\phi_{j+1,h} + \phi_{j-1,h} + \phi_{j,k+1} + \phi_{j,k-1}] = [S^y_{j,k-1} - S^y_{jk} + S^x_{j-1,k} - S^x_{jk}]h, \tag{2.7}$$

where

$$g_{jk} = \begin{cases} 2 & j = 1 \ or \ N; k = 1 \ or \ N \\ 3 & \begin{cases} j = 1 \ or \ N; k = 2 \ to \ N-1 \\ k = 1 \ or \ N; j = 2 \ to \ N-1 \end{cases} \\ 4 & otherwise, \end{cases}$$

SOR method generally promises improvement in convergence, although it needs a parameter *w* which maximizes the rate of convergence. The optimal value can be shown through the following equation,

$$\omega = \frac{2}{1+\sin\left[\frac{\pi}{(N+1)}\right]} \tag{2.8}$$

By using the optimal parameter and combine the method using Matlab 2009, we only need to perform 16 iterations to get zero rms error. The RMS wavefront reconstruction error can be calculated by comparing the wavefront reconstructed from the slopes with the simulated wavefront from the Hudgin formula. (Hudgin, 1977)

Different wavefront reconstruction technique has been developed over past few years. Some recent disclosure of the reconstruction technology is listed chronologically in Table 2.3.

Table 2.3 Reconstruction Method Review

Year	Author	Description
2005	Huanqing Guo	Modelling the gradients measured by wavefront sensor with the Fried geometry with iterative discrete Fourier transforms to reconstruct the wavefront.(Guo & Wang, 2006)
2009	Wu Wei Wei	A Shack Hartman sensor has been simulated virtually to be used to do wavefront reconstructed. Authors prove that with high aperture, with the 'simulated H-S' method , the wavefront can be reconstructed(WU, SUN, & SONG, 2009)
2009	M B Roopashree	Fourier and Vector Matrix Multiply reconstruction methods were used to reconstruct the Morte-Carlo simulated wavefront. It was observed that although Fourier reconstruction gave consistent accuracy when coherence length of wavefronts is larger than the corresponding pitch on the wavefront sensor, VMM method gives even better accuracy when the coherence length closely matches with the wavefront sensor pitch(Roopashree, Vyas, & Prasad, 2009)
2010	Julián Espinosa	A combined zonal and modal method that allows an accurate reconstruction of corneal surfaces has been proposed in the paper. (Espinosa, Mas, Pérez, & Illueca, 2010)

2.5 Review of multilayer inspection theory

Multilayer inspection theory currently is a hot topic in the research area. Light or laser, as a wave, it follow the wave propagation theory and can be developed into powerful inspection tool in the seismic area and semiconductor industry. It can improve the quality of wafer, cut down the total cost of inspection and increase the production time. Surface profile measurement can be find through Shack-Hartmann sensor, research about surface profile using wavefront sensing has been conducted by researchers in A-Star Singapore (Li, Zhao, Fang, Asundi, & Yin, 2008). Small perturbation theory (Franceschetti & Riccio, 2008) and 3D layer modeling (Lin, Zhang, & Fang, 2009) currently is trying to explain the multi layer structure. Mathematical 3D modeling has once been attempted for explanation of multilayer structure. (El-Shenawee, 2001) Li et al. and Lin et al. uses small perturbation and 3D layer modeling to establish high accuracy (nanometer) layer surface profiling. Besides open space optical application, wave transmission in bulk material like optical fibre ((Poxson et al., 2010) & (Schubert et al., 2008)) is useful for study when developed multilayer theory. Until today, multilayer surface profiling has not yet studied using wavefront approach.

Chapter 3

THE BASIC PLAN FOR DESIGN AND EXPERIEMENT

3.1 Optical System Design

Limited by financial constraint, a low cost optical system was built in the project to match 1st objective "Design an optical system which is able to do wafer surface inspection.

The hole array I make is 4x4 hole array, each hole size is 0.3mm as indicated in the figure.
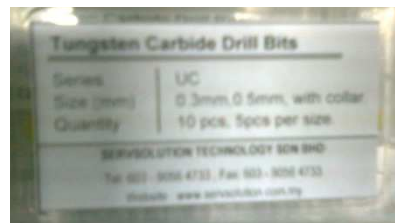
Figure 3.1 Tungsten Carbide Drill Bits Set
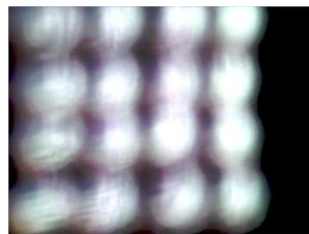
Figure 3.2 Hole Array

The theory behind this beam expander as shown below,
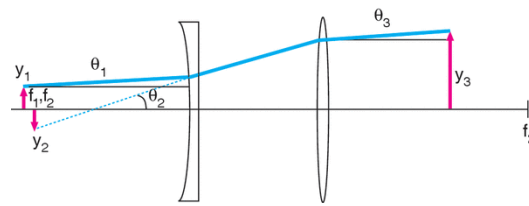
Figure 3.3 Focusing and Collimating.
Retrieved January 19, 2011, from
http://www.newport.com/store/genContent.aspx/Focusing-and
Collimating/141191/1033
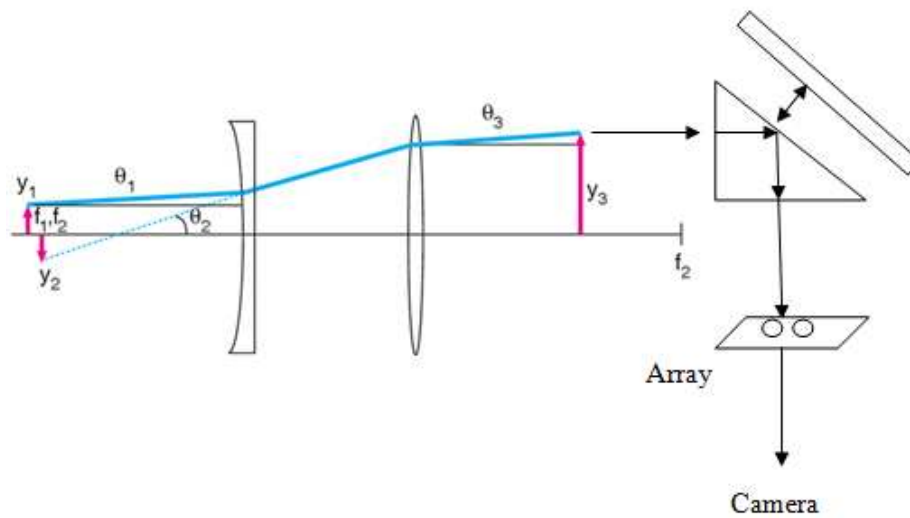
Figure 3.4 Conceptual Design

Above is the schematic of working principle of my optical system. so the light can pass through the hole array, By comparing the wavefront of mirror and the wafer, we can know defect of the wafer based on the wavefront reconstruction technique.

In my design, there are two lens used in the above design, one convex lens (Focal length = 250mm) and one concave lens (focal lengths=-150mm).Theoretically, a laser beam of radius y_1 and divergence θ_1 is expanded by a negative lens with focal length $-f_1$. In optical design, we know $\theta_2 = y_1/|-f_1|$, and the optical invariant tells us that the radius of the virtual image formed by this lens is $y_2 = \theta_1|-f_1|$. This image is at the focal point of the lens, $s_2 = -f_1$, because a well-collimated laser yields $s_1 \sim \infty$, so from the Gaussian lens equation $s_2 = f$. Adding a second lens with a positive focal

length f_2 and separating the two lenses by the sum of the two focal lengths $-f_1 + f_2$, results in a beam with a radius $y_3 = \theta_2 f_2$ and divergence angle $\theta_3 = y_2/f_2$.

The expansion ratio or the ratio of the focal lengths of the lenses is calculated in equation (9)

$$\frac{y_3}{y_1} = \frac{\theta_2 f_2}{\theta_2 |f_1|} = \frac{f_2}{|-f_1|} \tag{3.1}$$

The expanded beam diameter is calculated in equation (10)

$$2y_3 = 2\theta_2 f_2 = \frac{2y_1 f_2}{|-f_1|} \tag{3.2}$$

The divergence angle of the resulting expanded beam

$$\theta_3 = \frac{y_2}{f_2} = \frac{\theta_1 |-f_1|}{f_2} \tag{3.3}$$

is reduced from the original divergence by a factor that is equal to the ratio of the focal lengths $|-f1|/f2$. So, to expand a laser beam by a factor of five we would select two lenses whose focal lengths differ by a factor of five, and the divergence angle of the expanded beam would be 1/5th the original divergence angle.

In my design, refer to OS-8525A specification, the laser beam we use is HeNe laser with wavelength 650nm and beam diameter 3.5mm. After several measurement, divergence <2mrad, so we set it as 1.2 mrad. As the change is very small with limited space, the divergence measurement is tedious. According the spreadsheet I download from website and key in data, the divergence I measure is 380 mrad, indicate error caused by insufficient space. I make the assumption.

$$Y_1 = \frac{3.5}{2} = 1.75\text{mm, divergence } \theta_1 = 1.2\text{mrad.}$$

Use concave lens $f_1 = -150$mm and convex lens $f_1 = 250$mm, the spacing between the pair of lenses is actually the sum of the back focal lengths

$$BFL_1 + BFL_2 = -147 \text{ mm} + 247\text{mm} = 10 \text{ mm.}$$

Since real lenses differ in some degree from thin lenses. The expanded beam diameter

$$2y_3 = \frac{2y_1 f_2}{|-f_1|} = \frac{2(1.75mm)(250mm)}{|-150mm|} = 5.83mm \tag{3.4}$$

The divergence angle

$$\theta_3 = \frac{\theta_3|-f_1|}{f_2} = \frac{(1.2mrad)|-150mm|}{250mm} = 0.72mrad \qquad (3.5)$$

After constructing the beam expander to make a plane wave, I use a right angle prism to get the data.
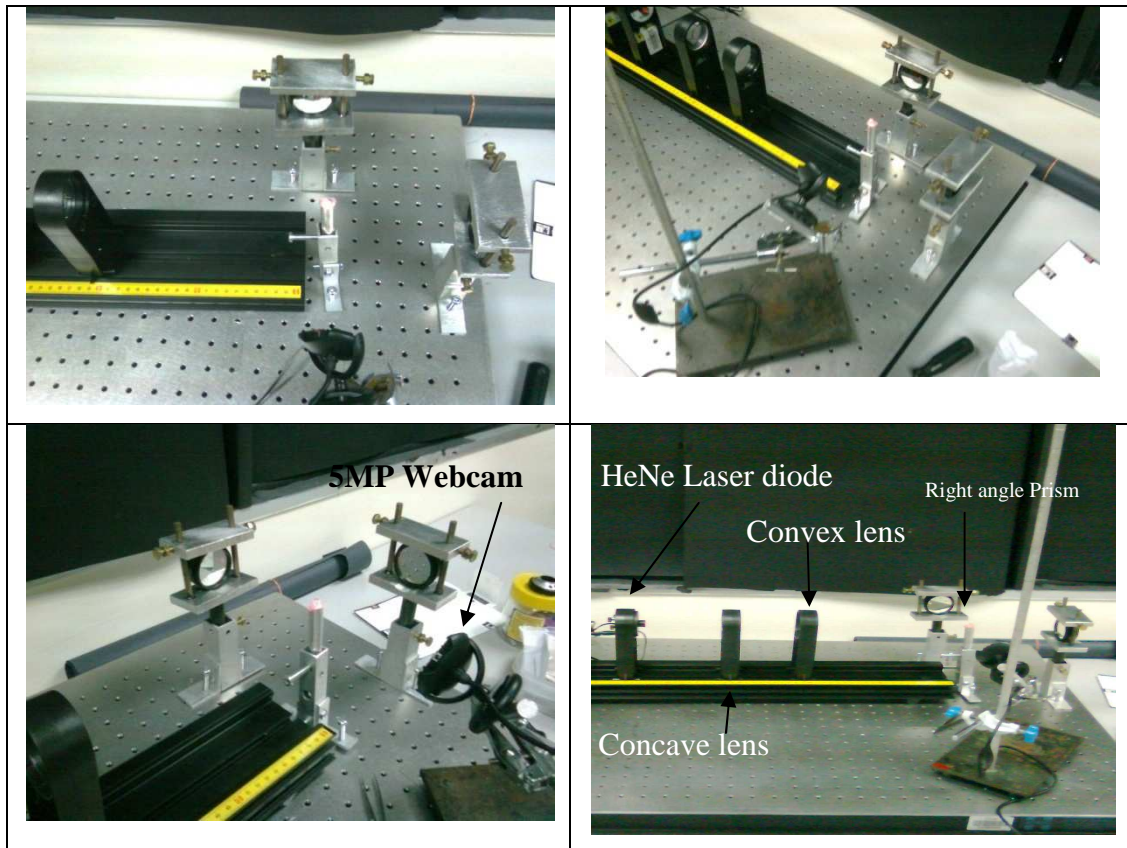
Figure 3.5 Different View of My Optical System

3.2 Experimental Setup

Before the experiment setup, we need to determine the focal length of the lens and build a beam expander.

I) Determination of focal length of a convex lens,

1. First place a convex lens of unknown focal length in the lens holder on the optical bench.

2. The optical bench is pointed to some distant bright objects, the distance is less than 50 meters.

3. A ground glass screen in its holder is placed on the optical bench and forms an image of the bright object. The difference between the readings of the lens holder and the ground glass screen holder will be the focal length of the lens.

4. A number of independent readings and average them for accuracy need to made.

II) Determination of focal length of concave lens

As indicated before, we need to complete the step 1and step 2, while in concave lens after step 2 above,

3. The ground glass screen needed to be adjusted until the bright object is in focus in front of convex lens.

4. The positions of the screen (S_1) are recorded down.

5. A concave lens of unknown focal length is placed between the convex lens and S_1
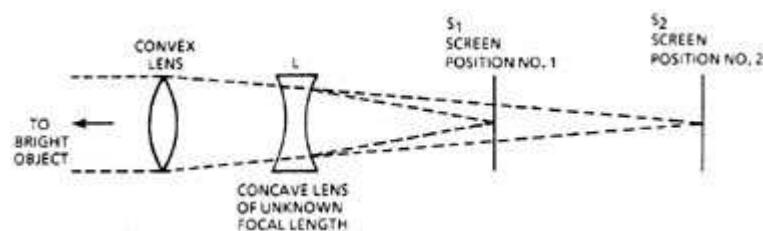
Figure 3.6 Determination of focal length of convex lens

6. Move the screen until the image is focus on the screen.

7. Use formula to calculate the focal length of the concave lenses.

$$\frac{1}{focal\ length} = \frac{1}{Distance\ LS_2} = \frac{1}{Distance\ LS_1}$$

8. Independent readings are taken for accuracy.

III) Build a beam expander.

To expand a laser beam, we need at least two lenses to complete it.

1. A laser beam of radius y1 and divergence θ1 need to be measured.

2. The laser is mounted in a fixed position and level the laser.

He-Ne Laser
632.8 nanometers

Original Beam diameter D₁

Diameter of beam on screen (D2)

S

S = distance from laser to screen
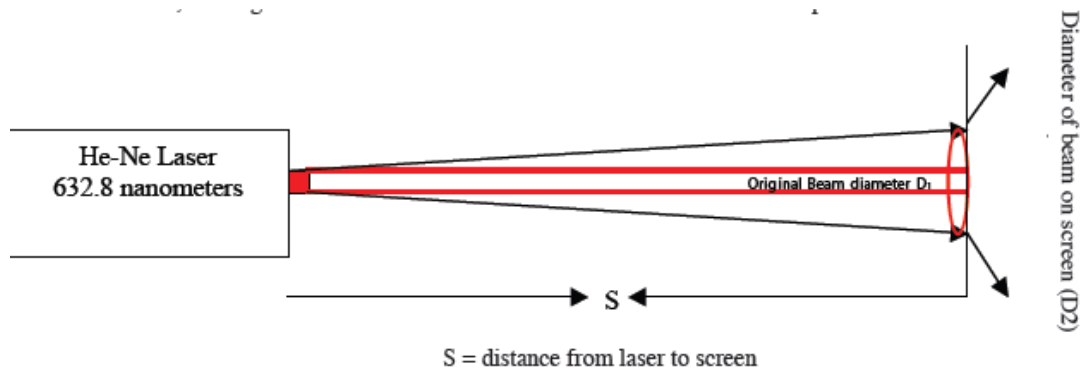
Figure 3.7 Layout for the Beam Divergence Measurement

3. A white screen is placed at various distances and carefully

Note: the outside dimensions of the laser pattern at seven different distances. Since the measurements involve the amount of divergence of the beam from the source, the original beam diameter must be subtracted out of each subsequent measurement.

4. Record the data and put into the following table at least three times.

Table 3.1 Divergence Recording Table

Distance to screen (S) (mm)	Original beam diameter (D1) (mm)	Screen pattern Diameter (D2) (mm)	Difference of D2 – D1 (D3) (mm)

4. Make a graph of D3 vs. S.

5. Determine the slope of the graph which is beam divergence in radians.

Once determine the beam divergence, we can build the beam expander.
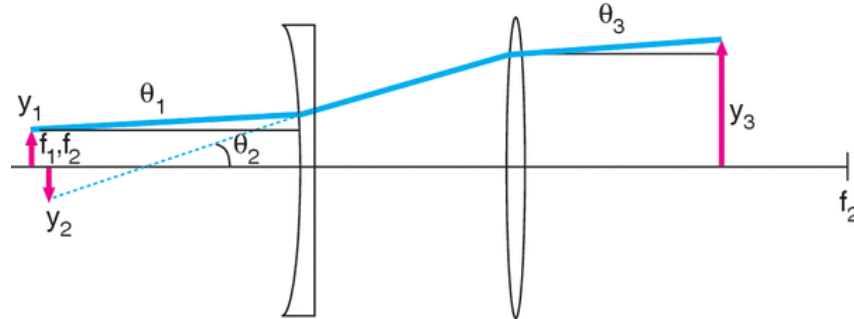
Figure 3.8 Beam Expander Illustrations

Extracted from http://www.newport.com/store/genContent.aspx/Focusing-and-Collimating/141191/1033, on 19th Jan 20111

A laser beam of radius y_1 and divergence θ_1 is expanded by a negative lens with focal length $-f_1$. Refer to the website, we know $\theta_2 = y_1/|-f_1|$, and the optical invariant tells us that the radius of the virtual image formed by this lens is $y_2 = \theta_1|-f_1|$. This image is at the focal point of the lens, $s_2 = -f_1$, because a well-collimated laser yields $s_1 \sim \infty$, so from the Gaussian lens equation $s_2 = f$. Adding a second lens with a positive focal length f_2 and separating the two lenses by the sum of the two focal lengths $-f_1 + f_2$, results in a beam with a radius $y_3 = \theta_2 f_2$ and divergence angle $\theta_3 = y_2/f_2$.

The expansion ratio

$$\frac{y_3}{y_1} = \frac{\theta_2 f_2}{\theta_2 |f_1|} = \frac{f_2}{|-f_1|} \tag{3.6}$$

or the ratio of the focal lengths of the lenses. The expanded beam diameter

$$2y_3 = 2\theta_2 f_2 = \frac{2y_1 f_2}{|-f_1|} \tag{3.7}$$

The divergence angle of the resulting expanded beam

$$\theta_3 = \frac{y_2}{f_2} = \frac{\theta_1 |-f_1|}{f_2} \tag{3.8}$$

is reduced from the original divergence by a factor that is equal to the ratio of the focal lengths $|-f_1|/f_2$. So, to expand a laser beam by a factor of five we would select two lenses whose focal lengths differ by a factor of five, and the divergence angle of the expanded beam would be 1/5th the original divergence angle.

Take real environment as an example, consider a HeNe laser with beam diameter $y_{1=}3.5mm$ (radius 3.5mm/2=1.75mm), and divergence θ_1=1mradians, negative lens focus length equal to -150mm (concave lens), $\theta_2 = y_1/|-f_1|= 1.75/150=0.01166$, $y_2 = \theta_1|-f_1|=1x150=150mm$, $s_2 = -f_1 = -150mm$, $s_1 \sim \infty$, $s_2 = f=250mm$, $L= -BfL_1 +BfL_2=-156.64+246.64=100mm$, $2y_3= 2y_1f_2/|-f_1|=2x1.75x250/|-150|=5.8333mm$. $\theta_3 = y_2/f_2 = \theta_1|-f_1|/f_2=1mrad$ x $|-150mm|/250=0.6mrad$.

6. Put the lens as indicated in figure, and measure the divergence with tools, the result should match with calculation result θ_3. if not, adjust the distance between two lens slowly. By using above step to select instrument, we manage to set up our optical system.

3.3 Basic Phase Reconstruction using Successive over Relaxation Method

Wavefront reconstruction is based on Southwell method (Southwell, 1980) or we may call it as zonal method which is widely applied

1. Create sample Wavefront Array based Hugin Formula (Hudgin, 1977)

$$W = \frac{2.3717(x^2-y^2)}{a^2} + \frac{6xy}{a^2} \tag{3.9}$$

where a= 1000µm (aperture size)

2. Generate sample X-slope and Y-slope

$$S = A\phi \tag{3.10}$$

S is a vector containing all the slope measurements(x slope and y slope)

ϕ vector of length N^2 containing all the unknown phase value

A is a rectangular matrix which size is N^2 by the number of slope measurement, can treat it as sparse matrix.

By multiplying equation (18) with A transpose, we get the equation

$$(A^+A)\phi = A^+S \tag{3.11}$$

Equation represents a set of N^2 linear equation in N^2 unknowns ϕ_{jk}

To solve the linear equation, we can add in a large sparse matrix to help us to perform the adjacent slope averaging so we can use iterative method to solve it.

$$(A^+A)\phi = A^+DS \tag{3.12}$$

By using Matlab to create sparse matrix and transpose matrix, and create a zero gradient wavefront, we can find the S_x and S_y from the equation.

3. Generate new wavefront array

$$g_{jk}\phi_{jk} - \left[\phi_{j+1,h} + \phi_{j-1,h} + \phi_{j,k+1} + \phi_{j,k-1}\right]$$
$$= \left[S^y_{j,k-1} - S^y_{jk} + S^x_{j-1,k} - S^x_{jk}\right]h, \tag{3.13}$$

where

$$g_{jk} = \begin{cases} 2 & j = 1\ or\ N; k = 1\ or\ N \\ 3 & \begin{cases} j = 1\ or\ N; k = 2\ to\ N-1 \\ k = 1\ or\ N; j = 2\ to\ N-1 \end{cases} \\ 4 & otherwise, \end{cases}$$

$h = \dfrac{d}{N}$, N is number of grid, d= distance between grid

To solve equation by iterative method, we call the right-hand side b_{jk}

$$\phi_{jk} = \overline{\phi_{Jk}} + \frac{b_{jk}}{g_{jk}} \tag{3.14}$$

where $\overline{\phi_{Jk}}$ is the nearest-neighbor phase average.

$$\overline{\phi_{Jk}} = \frac{\left[\phi_{j+1,k} + \phi_{j-1,k} + \phi_{j,k+1}\right]}{g_{jk}} \tag{3.15}$$

and

$$b_{jk} = \left[S^y_{j,k-1} - S^y_{jk} + S^x_{j-1,k} - S^x_{jk}\right]h \tag{3.16}$$

Equation forms the basis for an iterative solution

$$\phi_{jk}^{(m+1)} = \overline{\phi_{jk}^{(m)}} + \frac{b_{jk}}{g_{jk}} \tag{3.17}$$

Equation does not include ϕ_{jk} since $\overline{\phi_{jk}}$ does not include ϕ_{jk}

To include ϕ_{jk}, we use successive over relaxation method. We add and subtract the ϕ_{jk} on the right hand side and introducing the optimal relaxation parameter ω

$$\omega = \frac{2}{1+\sin[\frac{\pi}{N+1}]} \tag{3.18}$$

Thus the final equation for SOR method is

$$\phi_{jk}^{(m+1)} = \phi_{jk}^{(m)} + \omega[\overline{\phi_{jk}^{(m)}} + \frac{b_{jk}}{g_{jk}} - \phi_{jk}^{(m)}] \tag{3.19}$$

We apply the equation to reconstruct wavefront array.

3.4 Basic Centroiding

According to the (Yin, Li, Zhao, & Fang, 2009), most centroid detection methods have been proposed and analyzed from the point of view of optics. and the accuracy of the methods has been studied only by simulation.

In my project, instead of using conventional technique by adding gaussian distibution noise, I propose using blob measuremnt to detect the centroid of the image. The method is listed below which take Maltab "Marker-Controlled Watershed Segmentation" as reference.

Step 1: Read in the Color Image and Convert it to Grayscale

Step 2: Use the Gradient Magnitude as the Segmentation Function

In this step we use the Sobel edge masks, imfilter, and some simple arithmetic to compute the gradient magnitude. The gradient is high at the borders of the objects and low (mostly) inside the objects.

Step 3: Mark the white spot

We use reconstruction opening and closing to reconstruct the image. so it will not affect the overall shapes of the white spot. We also calculate the regional maxima of Iobrcbr to obtain good white spot markers.

Step 4:

Use regionprop to measure the centroids of each circle, this function will measure point out the centroids of connected binary object.

This method is useful to remove the uncertainly in the image as it employ sobel mask to filter out the noise in the image before centroiding the spot. It manages to eliminate various noises such as diffraction of the light, instability of the light source as well as deviation between the centroid of the spot and the center of the detection area. It is efficient to detect the white spot since it use less memory and cut down the overall time to proceed.

3.5 Build a Matlab GUI

This part we discuss on how to building a Graphical User Interface for wavefront surface profiling.
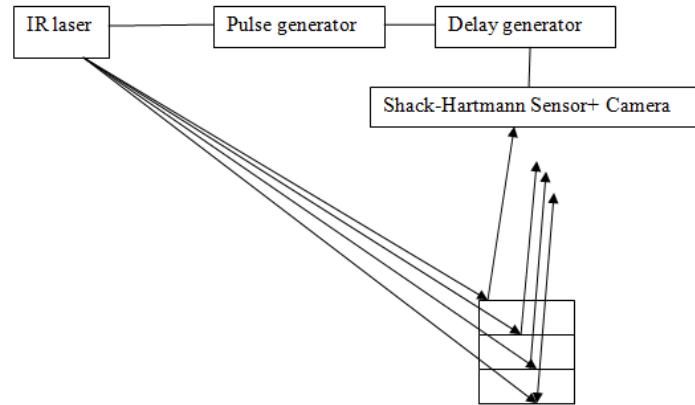
Figure 3.9 Multilayer Wavefront Sensing Illustration

Different layer will have time relay to reach the camera, so by capturing the coordinate layer by layer, we can extract surface profiling from it. From the final coordinate of first layer and final coordinate of second layer, we apply reconstruct technique to find the initial location of light input. If the reconstructed input location from first layer and second layer is the same, then we can conclude that the internal layer structure is good.
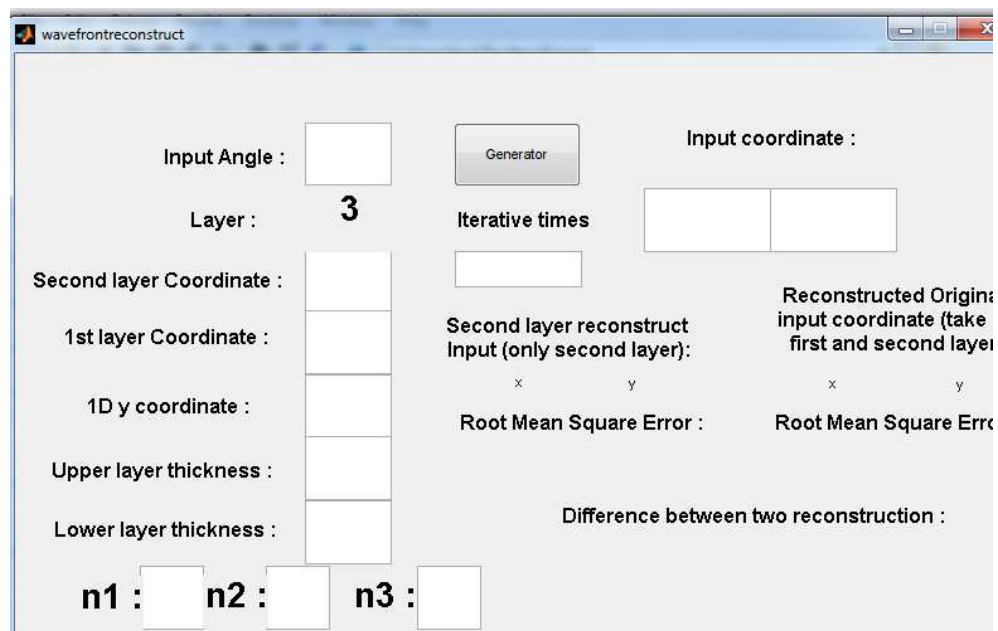
Figure 3.10 Matlab User Interface before Clicking Generator

A simple layout of my program user interface is shown above. Once the end-user click the generator button, it will generate the output based on the data in the white blank given.
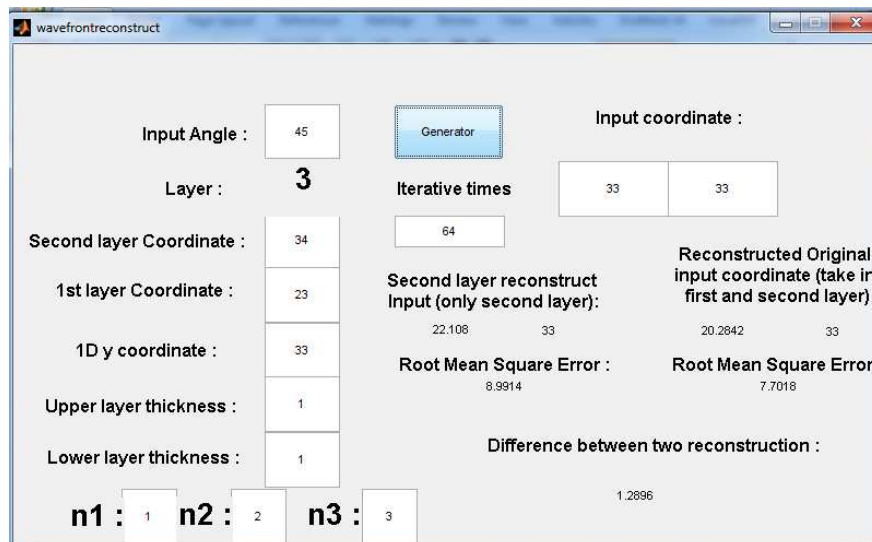
Figure 3.11 Matlab User Interface after Clicking Generator

End user is free to modify any data input to achieve the best result. By comparing the reconstruction input coordinate and original input coordinate, we manage to predict what kind of possible defect it may appear in the internal structure, the root mean square error of the two layer reconstruction as investigated below,

Table 3.2 Root Means Square Error of 1st Layer and 2nd Layer Reconstruction

1st layer output coordinate	Second layer output coordinate	Result difference Root means square error
35.805	45.915	0.2912
36.805	45.915	0.2191
37.805	45.915	0.1470
38.805	45.915	0.0748
39.805	45.915	0.0027
40.805	45.915	0.0694
41.805	45.915	0.1415
42.805	45.915	0.2136
43.805	45.915	0.2858
44.805	45.915	0.3579
45.805	45.915	0.4300

Chapter 4

GATED WAVEFRONT SENSING RECONSTRUTION

4.1 The challenge of multi-layer inspection theory

Currently research only can accomplish surface wavefront reconstruction task. However, the multilayer surface reconstruction is still a doubt. In this chapter, I develop a generic multilayer structure. Through study the generic multilayer structure, I manage to figure out four parameters which are helpful in the gated wavefront sensing. They are input angle, light intensity (power of light), location of light input and light output (absolute coordinate in one dimensional) and phase output for the Fresnel law. Total light intensity is indicated in figure.
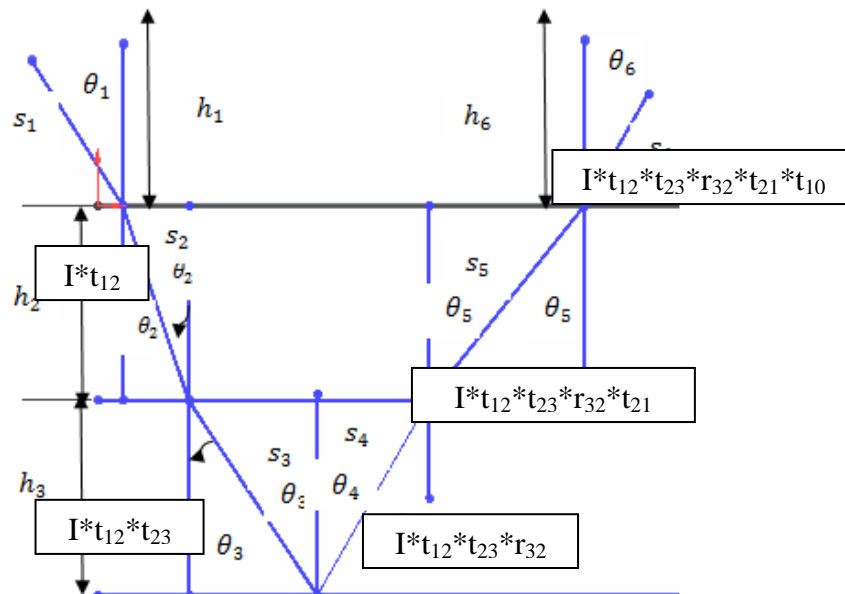
Figure 4.1 Illustrations for Optical Path Length for Light Output Intensity

Assume input power is 1000W

$W_1 = I * t_{12} = 308.5498W$

$W_2 = I * t_{12} * t_{23} = 288.7491W$

$W_3 = I * t_{12} * t_{23} * rr_{32} = 18.5301 \ W$

$W_T = W_1 * W_2 * W_3 = I * t_{12} * t_{23} * rr_{32} * rt_{21} = 31.3427W$

Results shows that the loss energy due to internal layer transmission.

In generic multilayer structure, we face the problem of the reflection and transmission of an electromagnetic plane wave at the interface between two medium. It can be solved by the Fresnel's formula with transfer matrix method in optics books.

Under 650nm red laser diode

Table 4.1   Refractive Index of Different Layer

Layer 1:Air n=1
Layer 2: Poly silicon n = 3.94028 *SOPRA N&K Database at 650nm*
Layer 3: Amorphous Silicon= 4.4643 *SOPRA N&K Database at 650nm*

To avoid confusion with other symbol, I use $\vec{\gamma}$ to express the incident plane wave vector in 3D domain. I divide it into $\vec{\gamma_x} = \vec{\gamma}cos\phi$ and $\vec{\gamma_y} = \vec{\gamma}sin\phi$ to further mathematical expression and processing. A nomenclature table is constructed as below
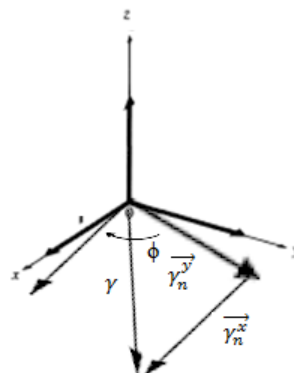
Figure 4.2 Illustration of x Direction and y Direction of Wave

If we use vector multiplication, we can get the z direction $\vec{\gamma}$, as in vector $i \cdot j = k$
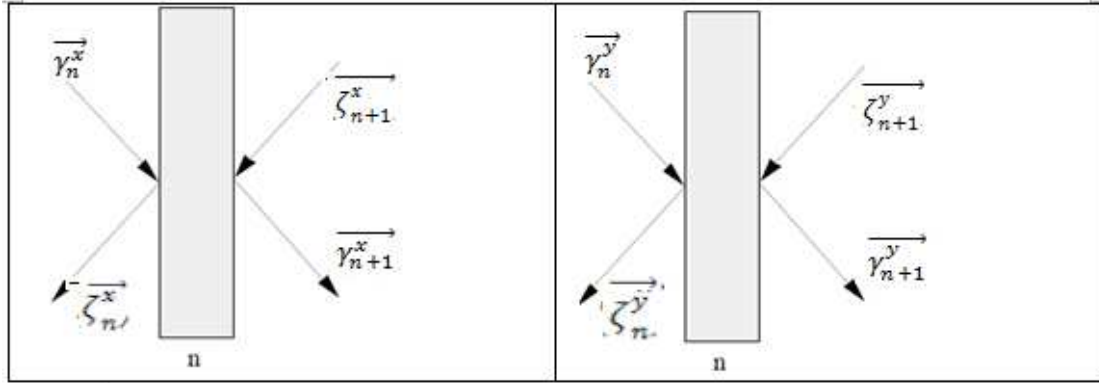
Figure 4.2 Illustrations of Reflection and Transmission

Thus, we have

$$\begin{pmatrix} \gamma_n^x \\ \zeta_n^x \end{pmatrix} = \widetilde{M}_m \begin{pmatrix} \gamma_{n+1}^x \\ \zeta_{n+1}^x \end{pmatrix} = \widetilde{M}_n \begin{pmatrix} \gamma_{n+1}^x \\ 0 \end{pmatrix} \tag{4.1}$$

$$\begin{pmatrix} \gamma_n^y \\ \zeta_n^y \end{pmatrix} = \widetilde{M}_m \begin{pmatrix} \gamma_{n+1}^y \\ \zeta_{n+1}^y \end{pmatrix} = \widetilde{M}_n \begin{pmatrix} \gamma_{n+1}^y \\ 0 \end{pmatrix} \tag{4.2}$$

In our consideration, we have 2 layers and semi-medium layer we set it as 0th layer, we assume the wave is reflected 100% in last layer.

To differentiate both M, we use $\widetilde{M}_m$ replace $\widetilde{M}_n$ in the first one.

where both $\widetilde{M}_m$ and $\widetilde{M}_n$ can be represented by the below equation

$$M = \frac{1}{t_{n-1,n}} \begin{pmatrix} e^{-i\delta_n} & r_{n-1,n}\, e^{-i\delta_n} \\ r_{n-1,n} e^{-i\delta_n} & e^{i\delta_n} \end{pmatrix} \tag{4.3}$$

We have two medium in which electromagnetic wave propagate, so the equation

$$\begin{aligned} \widetilde{M} &= \frac{1}{t_{12}} \begin{pmatrix} e^{-i\delta_2} & r_{12}\, e^{i\delta_2} \\ r_{12}e^{-i\delta_2} & e^{i\delta_2} \end{pmatrix} \frac{1}{t_{23}} \begin{pmatrix} 1 & r_{23} \\ r_{23} & 1 \end{pmatrix} \\ &= \frac{1}{t_{12}t_{23}} \begin{pmatrix} e^{-i\delta_2} + r_{12}\,r_{23}e^{i\delta_2} & e^{-i\delta_2}r_{23} + r_{12}\, e^{i\delta_2} \\ r_{12}e^{-i\delta_2} + e^{i\delta_2}r_{23} & r_{12}r_{23}e^{-i\delta_2} + e^{i\delta_2} \end{pmatrix} \end{aligned} \tag{4.4}$$

Similarly the application can be used on y direction wave propagation.

To study the propagation of wave inside the generic multilayer structure, we need to fill in all the t variable and r variable

The main basic equation for Fresnel law has four equations:

$$t_{ij}^s = \frac{2sin\alpha_j cos\alpha_i}{sin(\alpha_i+\alpha_j)} = \frac{2n_i cos\alpha_i}{n_i cos\alpha_i + n_j cos\alpha_j} \tag{4.5}$$

$$r_{ij}^s = -\frac{sin(\alpha_i-\alpha_j)}{sin(\alpha_i+\alpha_j)} = \frac{n_i cos\alpha_i - n_j cos\alpha_j}{n_i cos\alpha_i + n_j cos\alpha_j} \tag{4.6}$$

$$t_{ij}^p = \frac{2sin\alpha_j cos\alpha_i}{sin(\alpha_i+\alpha_j)cos(\alpha_i-\alpha_j)} = \frac{2n_i cos\alpha_i}{n_j cos\alpha_i + n_i cos\alpha_j} \tag{4.7}$$

$$r_{ij}^p = -\frac{tan(\alpha_i-\alpha_j)}{tan(\alpha_i+\alpha_j)} = \frac{n_j cos\alpha_i - n_i cos\alpha_j}{n_j cos\alpha_i + n_i cos\alpha_j} \tag{4.8}$$

Before total internal reflection happen, we have following equation table.

Table 4.2 Equation table (I)

X direction	Y direction
$t_{12}^s = \dfrac{2n_1 cos\alpha_1}{n_1 cos\alpha_1 + n_2 cos\alpha_2}$ $t_{23}^s = \dfrac{2n_2 cos\alpha_2}{n_1 cos\alpha_1 + n_2 cos\alpha_2}$	$t_{12}^s = \dfrac{2n_1 cos\beta_1}{n_1 cos\beta_1 + n_2 cos\beta_2}$ $t_{23}^s = \dfrac{2n_2 cos\beta_2}{n_2 cos\beta_2 + n_3 cos\beta_3}$
$r_{12}^s = \dfrac{n_1 cos\alpha_1 - n_2 cos\alpha_2}{n_1 cos\alpha_1 + n_2 cos\alpha_2}$ $r_{23}^s = \dfrac{n_2 cos\alpha_2 - n_3 cos\alpha_3}{n_2 cos\alpha_2 + n_3 cos\alpha_3}$	$r_{12}^s = \dfrac{n_1 cos\beta_1 - n_2 cos\beta_2}{n_1 cos\beta_1 + n_2 cos\beta_2}$ $r_{23}^s = \dfrac{n_2 cos\beta_2 - n_3 cos\beta_3}{n_2 cos\beta_2 + n_3 cos\beta_3}$
$t_{12}^p = \dfrac{2n_1 cos\alpha_1}{n_2 cos\alpha_1 + n_1 cos\alpha_2}$ $t_{23}^p = \dfrac{2n_2 cos\alpha_2}{n_3 cos\alpha_2 + n_2 cos\alpha_3}$	$t_{12}^p = \dfrac{2n_1 cos\beta_1}{n_2 cos\beta_1 + n_1 cos\beta_2}$ $t_{23}^p = \dfrac{2n_2 cos\beta_2}{n_3 cos\beta_2 + n_2 cos\beta_3}$
$r_{12}^p = \dfrac{n_2 cos\alpha_1 - n_1 cos\alpha_2}{n_2 cos\alpha_1 + n_1 cos\alpha_2}$ $r_{23}^p = \dfrac{n_3 cos\alpha_2 - n_2 cos\alpha_3}{n_3 cos\alpha_2 + n_2 cos\alpha_3}$	$r_{12}^p = \dfrac{n_2 cos\beta_1 - n_1 cos\beta_2}{n_2 cos\beta_1 + n_1 cos\beta_2}$ $r_{23}^p = \dfrac{n_3 cos\beta_2 - n_2 cos\beta_3}{n_3 cos\beta_2 + n_2 cos\beta_3}$

Table 4.3 Equation Table (II)

X direction	Y direction
M_F for forward direction	M_F for forward direction
$$M_{11} = \frac{e^{-i\delta_2} + r_{12}\,r_{23}e^{i\delta_2}}{t_{12}t_{23}}$$ $$M_{21} = \frac{r_{12}e^{-i\delta_2} + e^{i\delta_2}r_{23}}{t_{12}t_{23}}$$	$$M_{11} = \frac{e^{-i\delta_2} + r_{12}\,r_{23}e^{i\delta_2}}{t_{12}t_{23}}$$ $$M_{21} = \frac{r_{12}e^{-i\delta_2} + e^{i\delta_2}r_{23}}{t_{12}t_{23}}$$
$$t = \frac{x_{N+1}}{x_1} = \frac{1}{M_{11}}$$ $$r = \frac{y_1}{x_1} = \frac{M_{21}}{M_{11}}$$	$$t = \frac{x_{N+1}}{x_1} = \frac{1}{M_{11}}$$ $$r = \frac{y_1}{x_1} = \frac{M_{21}}{M_{11}}$$
$$t^x = \frac{e^{i\delta_2}t_{12}t_{23}}{1 + r_{12}\,r_{23}e^{2i\delta_2}}$$ $$r^x = \frac{r_{12} + e^{i2\delta_2}r_{23}}{1 + r_{12}\,r_{23}e^{i2\delta_2}}$$	$$t^y = \frac{e^{-i\delta_2}\,t_{32}t_{21}}{1 + r_{21}\,r_{32}e^{2i\delta_2}}$$ $$r^y = \frac{r_{32} + r_{21}e^{2i\delta_2}}{1 + r_{32}\,r_{21}e^{i2\delta_2}}$$

Once it reach the 3rd layer we assume the light will have total internal reflection, whereby the $n_3 > n_2$, $\theta_r = \theta_i$.

so we reverse all the formula

After total internal reflection, we have equation table 4.3

Table 4.4 Equation table (III)

X direction	Y direction
$$t^s_{32} = \frac{2n_3 cos\alpha_3}{n_3 cos\alpha_3 + n_2 cos\alpha_2}$$ $$t^s_{21} = \frac{2n_2 cos\alpha_2}{n_2 cos\alpha_2 + n_1 cos\alpha_1}$$	$$t^s_{32} = \frac{2n_3 cos\beta_3}{n_3 cos\beta_3 + n_2 cos\beta_2}$$ $$t^s_{21} = \frac{2n_2 cos\beta_2}{n_2 cos\beta_2 + n_1 cos\beta_1}$$
$$r^s_{32} = \frac{n_3 cos\alpha_3 - n_2 cos\alpha_2}{n_3 cos\alpha_3 + n_2 cos\alpha_2}$$ $$r^s_{21} = \frac{n_2 cos\alpha_2 - n_1 cos\alpha_1}{n_2 cos\alpha_2 + n_1 cos\alpha_1}$$	$$r^s_{32} = \frac{n_3 cos\beta_3 - n_2 cos\beta_2}{n_3 cos\beta_3 + n_2 cos\beta_2}$$ $$r^s_{21} = \frac{n_2 cos\beta_2 - n_1 cos\beta_1}{n_2 cos\beta_2 + n_1 cos\beta_1}$$
$$t^p_{32} = \frac{2n_3 cos\alpha_3}{n_2 cos\alpha_3 + n_3 cos\alpha_2}$$ $$t^p_{21} = \frac{2n_2 cos\alpha_2}{n_1 cos\alpha_2 + n_2 cos\alpha_1}$$	$$t^p_{32} = \frac{2n_3 cos\beta_3}{n_2 cos\beta_3 + n_3 cos\beta_2}$$ $$t^p_{21} = \frac{2n_2 cos\beta_2}{n_1 cos\beta_2 + n_2 cos\beta_1}$$
$$r^p_{32} = \frac{n_2 cos\alpha_3 - n_3 cos\alpha_2}{n_2 cos\alpha_3 + n_3 cos\alpha_2}$$ $$r^p_{21} = \frac{n_1 cos\alpha_2 - n_2 cos\alpha_1}{n_1 cos\alpha_2 + n_2 cos\alpha_1}$$	$$r^p_{32} = \frac{n_2 cos\beta_3 - n_3 cos\beta_2}{n_2 cos\beta_3 + n_3 cos\beta_2}$$ $$r^p_{21} = \frac{n_1 cos\beta_2 - n_2 cos\beta_1}{n_1 cos\beta_2 + n_2 cos\beta_1}$$

Table 4.5 Equation Table (IV)

X direction	Y direction
M_R for reverse direction	M_R for reverse direction

$$\widetilde{M} = \frac{1}{t_{32}}\begin{pmatrix} e^{-i\delta_2} & r_{32}\,e^{i\delta_2} \\ r_{32}e^{-i\delta_2} & e^{i\delta_2} \end{pmatrix}\frac{1}{t_{21}}\begin{pmatrix} 1 & r_{21} \\ r_{21} & 1 \end{pmatrix}$$

$$= \frac{1}{t_{32}t_{21}}\begin{pmatrix} e^{-i\delta_2} + r_{32}\,r_{21}e^{i\delta_2} & e^{-i\delta_2}r_{32} + r_{21}\,e^{i\delta_2} \\ r_{32}e^{-i\delta_2} + e^{i\delta_2}r_{21} & r_{32}r_{21}e^{-i\delta_2} + e^{i\delta_2} \end{pmatrix}$$

$$M_{11}{}' = \frac{e^{-i\delta_2} + r_{32}\,r_{21}e^{i\delta_2}}{t_{32}t_{21}}$$

$$M_{21}{}' = \frac{r_{32}e^{-i\delta_2} + e^{i\delta_2}r_{21}}{t_{32}t_{21}}$$

$$t = \frac{x_{N+1}}{x_1} = \frac{1}{M_{11}}$$

$$r = \frac{y_1}{x_1} = \frac{M_{21}}{M_{11}}$$

$$t^x = \frac{e^{-i\delta_2}\,t_{32}t_{21}}{1 + r_{12}\,r_{23}e^{2i\delta_2}}$$

$$r^x = \frac{r_{32} + r_{21}e^{2i\delta_2}}{1 + r_{32}\,r_{21}e^{i2\delta_2}}$$

Y direction:

$$\widetilde{M} = \frac{1}{t_{32}}\begin{pmatrix} e^{-i\delta_2} & r_{32}\,e^{i\delta_2} \\ r_{32}e^{-i\delta_2} & e^{i\delta_2} \end{pmatrix}\frac{1}{t_{21}}\begin{pmatrix} 1 & r_{21} \\ r_{21} & 1 \end{pmatrix}$$

$$= \frac{1}{t_{32}t_{21}}\begin{pmatrix} e^{-i\delta_2} + r_{32}\,r_{21}e^{i\delta_2} & e^{-i\delta_2}r_{32} + r_{21}\,e^{i\delta_2} \\ r_{32}e^{-i\delta_2} + e^{i\delta_2}r_{21} & r_{32}r_{21}e^{-i\delta_2} + e^{i\delta_2} \end{pmatrix}$$

$$M_{11}{}' = \frac{e^{-i\delta_2} + r_{32}\,r_{21}e^{i\delta_2}}{t_{32}t_{21}}$$

$$M_{21}{}' = \frac{r_{32}e^{-i\delta_2} + e^{i\delta_2}r_{21}}{t_{32}t_{21}}$$

$$t = \frac{x_{N+1}}{x_1} = \frac{1}{M_{11}}$$

$$r = \frac{y_1}{x_1} = \frac{M_{21}}{M_{11}}$$

$$t^x = \frac{e^{-i\delta_2}\,t_{32}t_{21}}{1 + r_{12}\,r_{23}e^{2i\delta_2}}$$

$$r^x = \frac{r_{32} + r_{21}e^{2i\delta_2}}{1 + r_{32}\,r_{21}e^{i2\delta_2}}$$

Combine both M in forward direction and reverse direction

Table 4.6 Equation Table (V)

X direction	Y direction
$M_m = M_F \cdot M_R$ $= M_{11} \cdot M_{21} \cdot M_{11}{}' \cdot M_{21}{}'$	$M_n = M_F \cdot M_R$ $= M_{11} \cdot M_{21} \cdot M_{11}{}' \cdot M_{21}{}'$

Recall back we have following relationship between input wave and output wave

$$\begin{pmatrix} \gamma_n^x \\ \zeta_n^x \end{pmatrix} = \widetilde{M}_m \begin{pmatrix} \gamma_{n+1}^x \\ \zeta_{n+1}^x \end{pmatrix} = \widetilde{M}_m \begin{pmatrix} \gamma_{n+1}^x \\ 0 \end{pmatrix} \tag{4.9}$$

$$\begin{pmatrix} \gamma_n^y \\ \zeta_n^y \end{pmatrix} = \widetilde{M}_m \begin{pmatrix} \gamma_{n+1}^y \\ \zeta_{n+1}^y \end{pmatrix} = \widetilde{M}_n \begin{pmatrix} \gamma_{n+1}^y \\ 0 \end{pmatrix} \tag{4.10}$$

Once we have the expression function of planar wave, in typical optic book, we define the planar wave as

$$\gamma_n^x = \Psi(\vec{r}, t) = A e^{i(\vec{k}\cdot\vec{r}\pm\omega t)} \tag{4.11}$$

where A =amplitude   ω: pulsation of all wave   k : constant parameter

We can express the final output wave in exponential form, so by applying in real case, through many times of trial run, we can estimate the constant parameter for the equation, and predict the time of wave propagation in generic multilayer structure.

We also perform one optical path length calculation
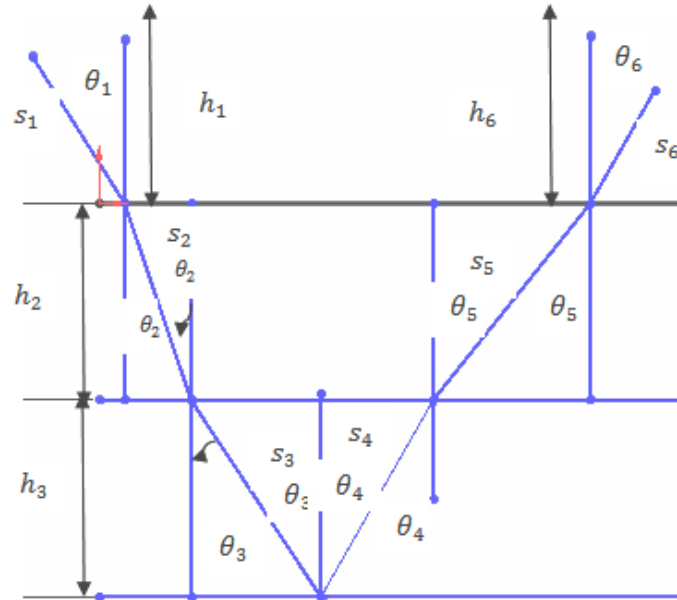
Figure 4.4 Illustration of Optical Path Length s

$$cos\theta_1 = \frac{h_1}{s_1} \tag{4.12}$$

$$s_1 = \frac{h_1}{cos\theta_1} \tag{4.13}$$

h_1 is the distance from light source to wafer surface,
h_6 is the distance from wafer surface to the detector.
Following the above equation,
Spatial optical path length

$$\sum_{i=1}^{m} s_i = \sum_{1}^{m} \frac{h_i}{cos\theta_i} \tag{4.14}$$

while $n_i sin\theta_i = n_{i+1} sin\theta_{i+1}$.In the other way, the optical path length traversed by the ray can be expressed as

$$\sum_{i=1}^{m} n_i s_i = \sum_{i=1}^{m} n_i \frac{h_i}{cos\theta_i} \tag{4.15}$$

The total time needed can be counted using equation below

$$t = \frac{1}{c}\sum_{i=1}^{m} n_i s_i \qquad (4.16)$$

4.2 Application of Southwell method to Fresnel-s polarization wave and p-polarization wave

I write a Maltab code for automatically calculate s-polarization and p-polarization wave. Assume 45° for input angle, 3 layers. For conventional method to calculate the wave propagation in the theory we develop, we need to use amplitude measurement to get the phase data or use phase $\delta = (2\pi d/\lambda)*n*\cos \theta$ where we need to know the thickness d and wavelength λ to calculate it.

We develop a new way by measure the centroiding coordinate to get the phase data. After that, by using reconstructed phase data extracted from the experimented image, we can generate all the wave value. Currently I do it manually, in the future, when Maltab new version which can output multiple matrixes, we can do it automatically.

Chapter 5

RESULT AND DISCUSSION

5.1 Comparison of centroiding of two images

In this chapter, I show the experimental image and how my theory work in experiment. First of all, I compare the Gaussian distribution of one hole and multiple holes array.
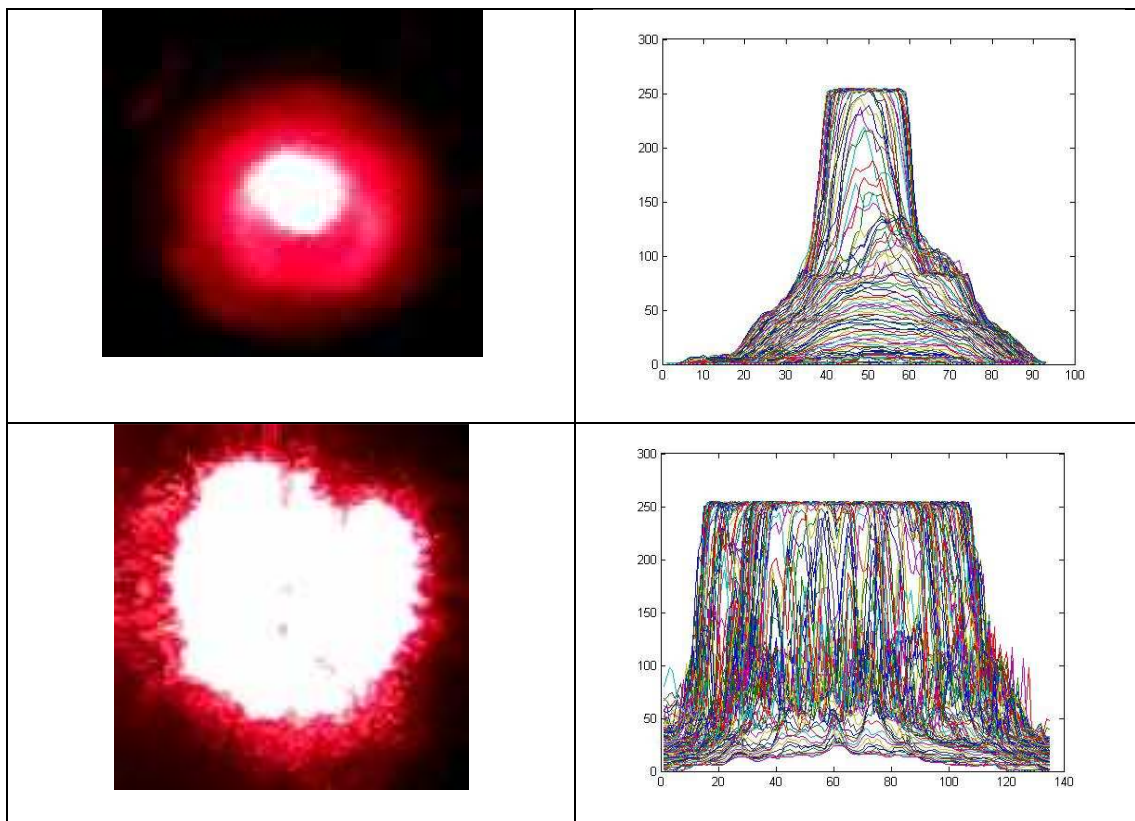
Figure 5.1 Comparison of Original Hole and After Hole Array Gaussian Distribution

The diffraction effect results the Gaussian distribution of the light become wide in the second figure. The noise appear in the hole array image, it become obvious in the hole array, as the light intensity has been distributed on the hole array and some absorption and excitation of electron may cause the noise. I once tried to add in the Gaussian noise into the image follow the conventional technique but the final outcome lack of accuracy.

Gaussian noise appears in most digital image since most noise can converted into normal distribution noise. By applying wiener filter to remove Gaussian noise of image, we are able to standardize the image and spot the uniform circuit. When we add noise to our image, result is not so good, as original image already consist Gaussian distribution noise.
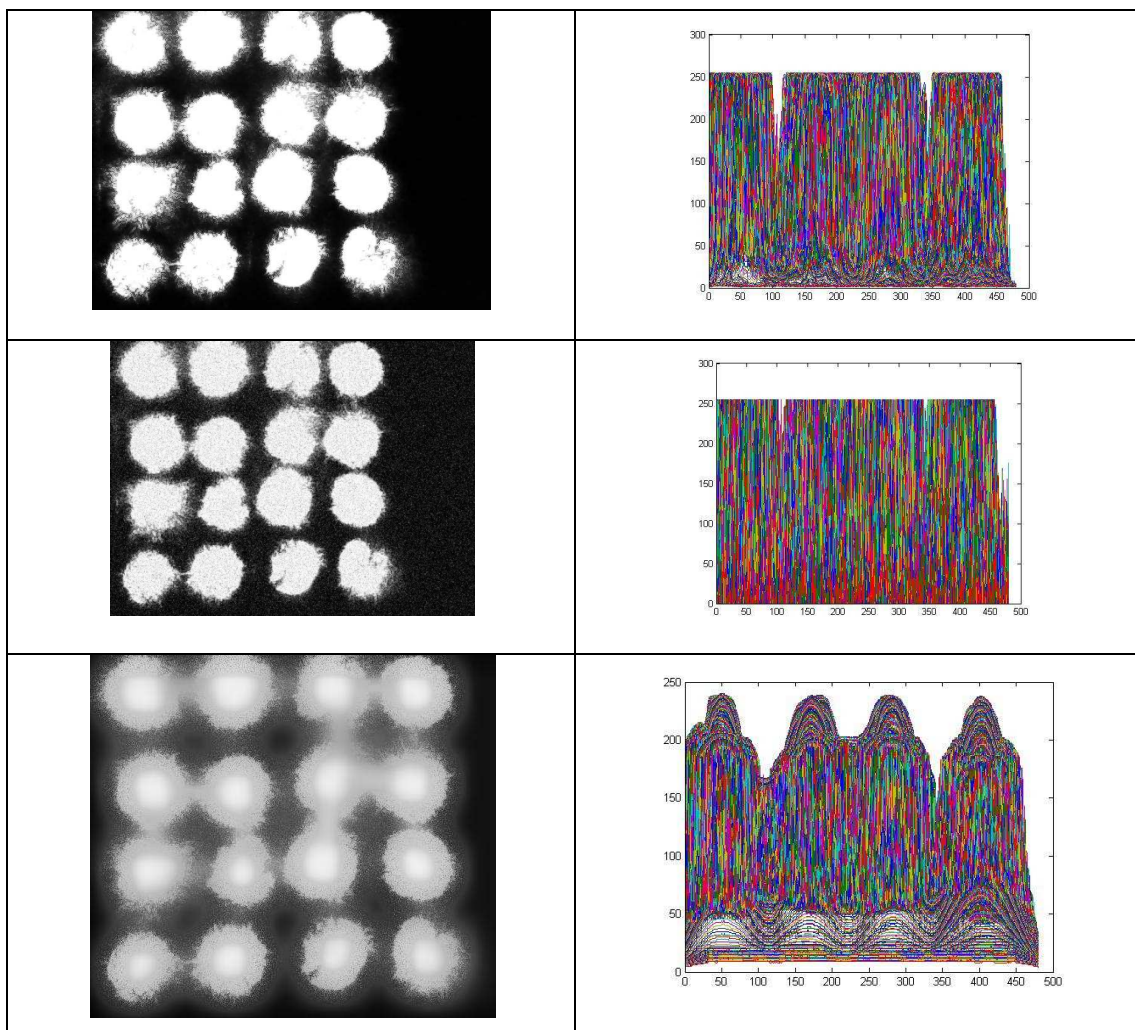
Figure 5.2   Image Processing

Instead of adding Gaussian noise, I directly remove Gaussian noise from the image by one kind of adaptive filter, Wiener filter. After that I apply watershed to do segmentation and get the centroids.

Figure 5.3   Centroiding
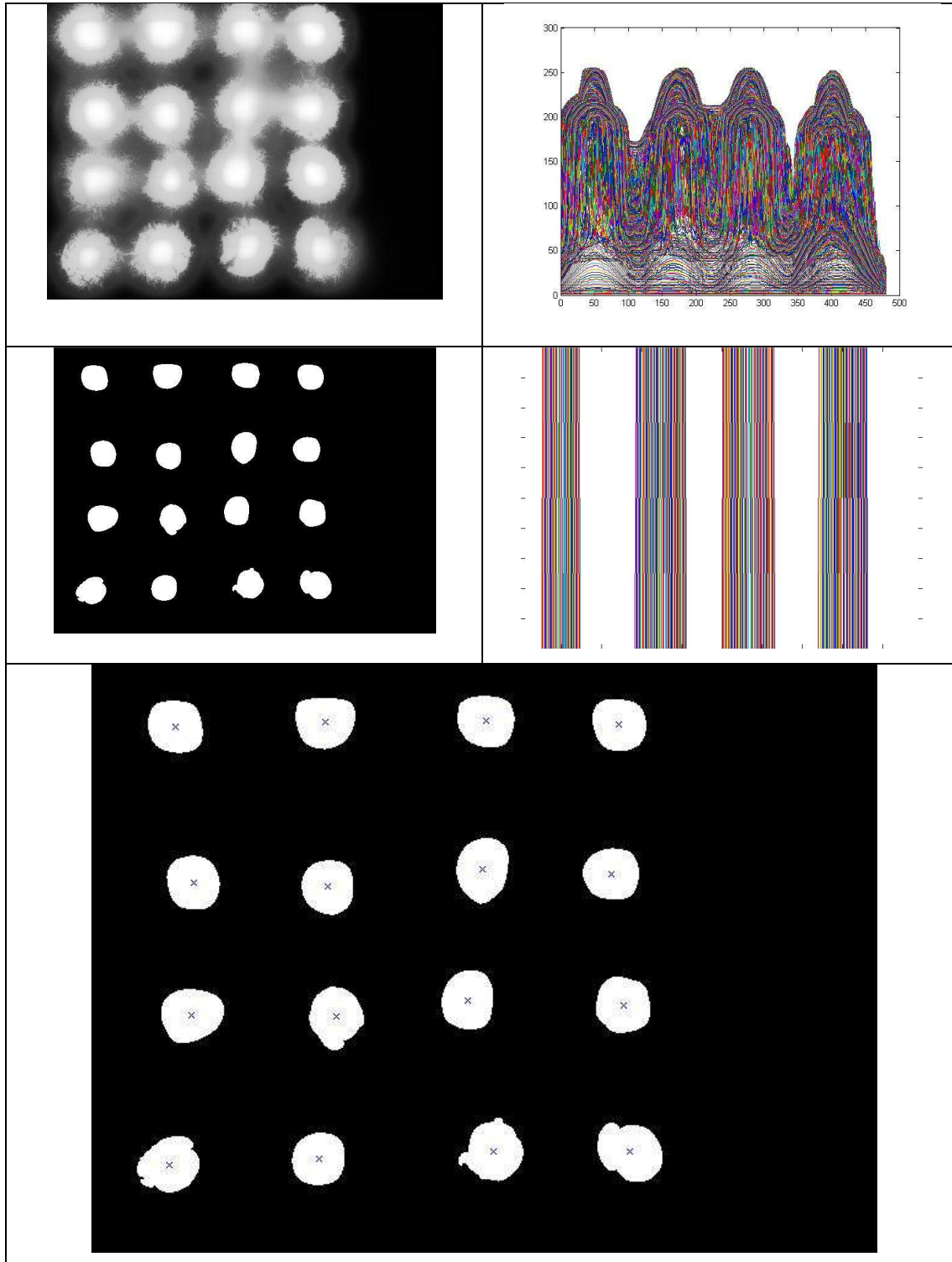
Before Centroiding	After centroiding
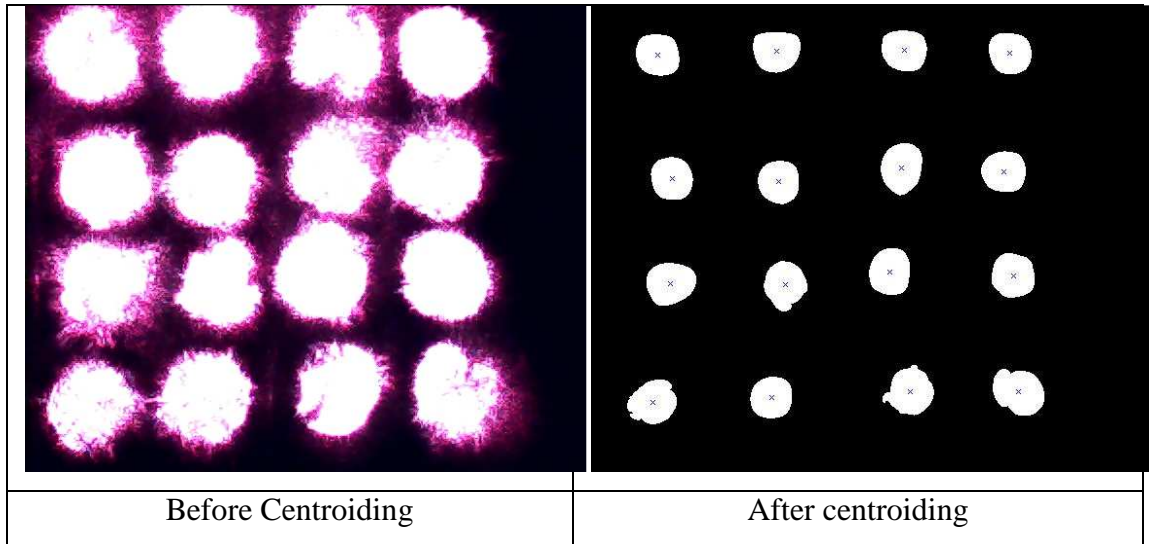
Figure 5.4   Comparison of Before Centroiding and After Centroiding

After centroiding both image, I use my user interface to get the center coordinate to calculate slope from both experimental image and simulated image as listed below.

Figure 5.5 Experimental Image

Figure 5.6 Sample Image

$$Sx = \frac{(x1-x2)}{f} \qquad (5.1)$$

$$Sy = \frac{(y1-y2)}{f} \qquad (5.2)$$

Sx is x-slope

Sy is y-slope

[x1,y1] is experimental image coordinate [x,y]

[x2,y2] is simulated image coordinate[x,y]

f is distance between hole array and CCD chip,250µm.

Data is listed below,

For experimental image

Table 5.1 X Coordinate and Y Coordinate of Experimental Image Centroiding

X coordinate					Y coordinate			
69.7486	69.0897	80.6957	82.9408		51.0362	411.9959	281.3856	178.2926
185.8276	191.1115	193.3309	202.4822		404.5826	47.3989	181.8783	288.2836
307.7336	322.2697	318.4843	325.9241		275.3945	44.5633	165.7246	395.0686
425.5206	430.6672	434.2049	445.4405		171.3468	49.1074	278.186	399.9777

For Simulated image

Table 5.2 X Coordinate and Y Coordinate of Simulated Image Centroiding

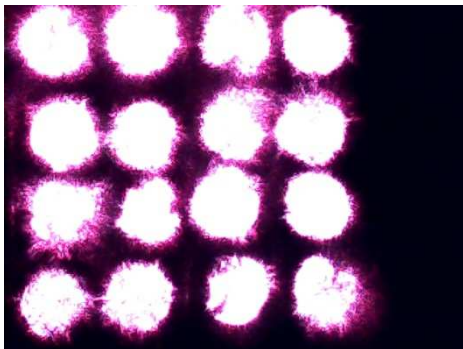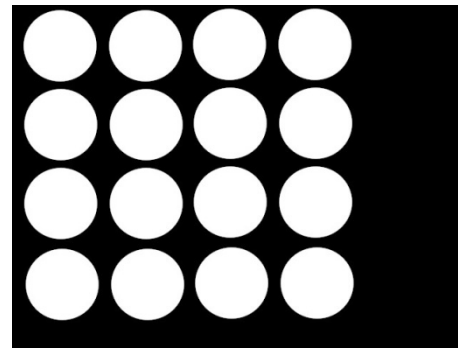| X coordinate					Y coordinate			
67.9948	69	69	71.0052		58.0036	169	280	394.0036
187.9948	189	189	191.0052		58.0036	169	280	394.0036
306.0007	307.0002	307.0063	309		56.0062	166.9932	277.9993	392
426.0007	427.0002	427.0063	429		56.0062	166.9932	277.9993	392

The slope and coordinate data will be used in next section for phase reconstruction.

Table 5.3 Refractive Index of Different Layers

Layer 1:Air n=1
Layer 2: Poly silicon n = 3.94028   *SOPRA N&K Database at 650nm*
Layer 3: Amorphous Silicon= 4.4643   *SOPRA N&K Database at 650nm*

Based on the above 3 index data, input angle is 45 degree (after right angle prism), assume the thickness of object is 1mm, and lower thickness is 1mm, (total thickness of subject is 2mm), we use excel and our Matlab user interface, reconstruct coordinate one by one, and put in table form, the initial coordinate after using the output image coordinate.

Table 5.4 Second Layer Reconstruct X Coordinate and Y Coordinate

Second layer reconstruct X coordinate				Reconstructed Y coordinate			
49.0453	50.0505	50.0505	52.0557	39.0568	150.0505	261.0505	375.0541
169.0453	170.0505	170.0505	172.0557	39.0568	150.0505	261.0505	375.0541
287.0512	288.0507	288.0568	290.0505	37.0567	148.0437	259.0428	373.0505
407.0512	240.6358	408.0568	410.0505	37.0567	148.0437	259.0428	373.0505

5.2 Plotting 3D surface profile

We have experimental data generated by the simple optical system. Running through 64 iteration by setting the f (length between array and camera) =1000000(1µm) using SOR method, the width of aperture as 0.1nm (This is only assumption, as the hole array has defect and affect light pass through) our phase value ϕ

Table 5.5   Reconstructed Phase Value

-0.15165	0.013719	-0.00834	0.005067
0.181136	-0.01667	0.010133	-0.00616
-0.18114	0.016672	-0.01013	0.006157
0.151645	-0.01372	0.008338	-0.00507

Compare original wavefront and reconstructed wavefront and get the root mean square error

Before wavefront reconstruction	After wavefront reconstruction
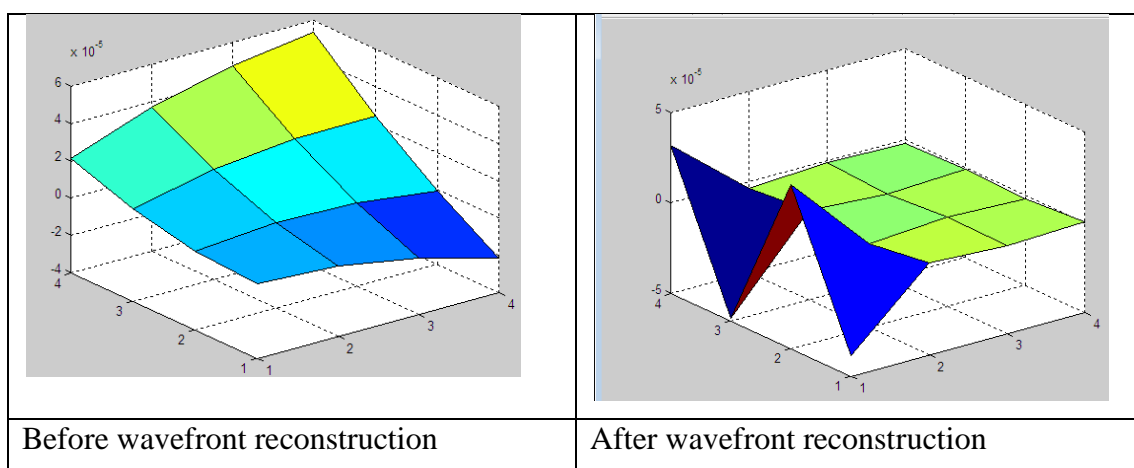
Figure 5.7 Comparison of 3D Plot Before Wavefront Reconstruction and After Wavefront Reconstruction

Root mean square error = 8.4741e-005

Combining phase value and centroiding coordinate of the original image, 3D plot can be generated. The idea behind the 3D plot using Maltab is we first plot out x center coordinate matrix and y center coordinate matrix to come out a 2D plot, and later we add in phase data to create a 3D plot.
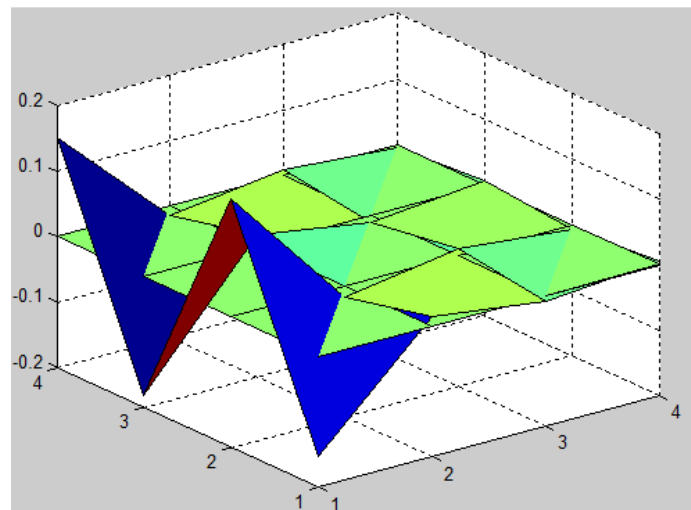
Figure 5.8 Combinations of Centroiding Data and Phase Data of Output Surface

Based on the surface profile of output image, now we use backprojection algorithm to figure out the internal layer surface profile by using the experimental coordinate.

5.3 Multilayer reconstruction result based on numerical model

Table 5.6 Refractive Index of Different Layers

Layer 1:Air n=1
Layer 2: Poly silicon n = 3.94028   *SOPRA N&K Database at 650nm*
Layer 3: Amorphous Silicon= 4.4643   *SOPRA N&K Database at 650nm*

Based on the index above, we use the Snell law to get necessary parameter for our generic multilayer structure.

Table 5.7   Snell Law Calculation (2)

	input angle	n1	sinx1	n2	sin x2	Angle output
AIR TO POLYSILICON	45	1	0.707106781	3.94028	0.179455973	10.33807338
polySi-Si	10.33807338	3.94028	0.179455973	4.4643	0.158391412	9.113540351
Si-Air	9.113540351	4.4643	0.158391412	1	0.707106781	45

We take the reflected angle as 45°, as input angle for the reverse direction, in Snell's law

Table 5.8   Snell Law Calculation (3)

	input angle	n1	sinx1	n2	sin x2	Angle output
Air to Si	45	1	0.707106781	4.4643	0.158391412	9.113540351
Si to polySi	9.113540351	4.4643	0.158391412	3.94028	0.179455973	10.33807338
polySi to air	10.33807338	3.94028	0.179455973	1	0.707106781	45

From layer 1 to layer 3,

Table 5.9   Result of Multilayer Theory (1)

	i=n			
θ1	θ2	θ3		
45	10.338073	9.11354		
	j=n			
θ1	θ2	θ3		
10.33807	9.11354	45		
	n			
n1	n2	n3		
3.94028	4.4643	1		
S-polarization			P-polarization	
t12	-6.28772		t12	-65.847
t23	1.482671		t23	1.122543
r12	-7.28772		r12	-75.6041
r23	0.482671		r23	-0.74855

From layer 3 to layer 1

Table 5.10   Result of Multilayer Theory (2)

	i=n			
θ1	θ2	θ3		
45	9.11354	10.33807		
	j=n			
θ1	θ2	θ3		
9.11354	10.33807	45		
	n			
n1	n2	n3		
4.4643	3.94028	1		
S-polarization			P-polarization	
t32	0.404835		t32	-0.32572
t21	76.60408		t21	0.280204
r32	-1.32572		r32	-0.59516
r21	75.60408		r21	-7.28772

Take the incident angle for x component and y component wave $\alpha = \beta = 45°$ and we only focus on final wave output t and r.
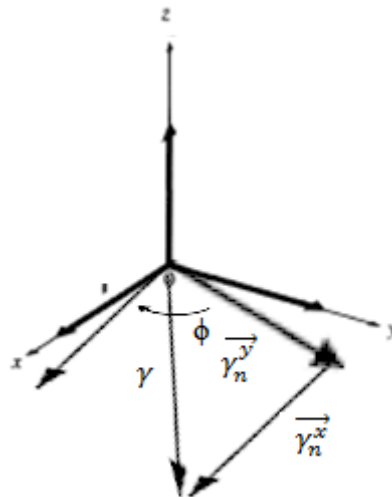
Wave Direction as shown next page,

Figure 5.9 Illustration of x Direction and y Direction of Wave

Table 5.11 Result of Optical Path length

Angle (°)	θ1	θ2	θ3	θ4	θ5	θ6
	30	7.242589	20.02717	20.02717	7.242589	30
Thickness	h1	h2	h3	h4	h5	h6
(micrometer)	5	5	5	5	5	5
OPL	s1	s2	s3	s4	s5	s6
	5.773503	5.040215	5.321808	5.321808	5.040215	5.773503
Refractive index	n1	n2	n3	n4	n5	n6
	1	4.2874	3.4213	3.4213	4.2874	1
	n1*s1	n2*s2	n3*s3	n4*s4	n5*s5	n6*s6
	5.773503	21.60942	18.2075	18.2075	21.60942	5.773503
sum of s	32.27105 µm					
sum of ns	91.18084µm					

5.4 Verification of phase reconstruction algorithm with Zernike Reconstruction result

Following Dai Guang Min algorithm (Dai, 2008), the author attaches the Zernike Polynomial algorithm into the book. I use it to verify the validity of my algorithm.

A zero gradient matrix is created in the Matlab. I use the zero gradient matrixes to reconstruct a wavefront from the measured wavefront gradients. After that, I compare the reconstructed wavefront and the zero gradient matrixes. It returns a root means square error 0.084.

To formulate Zernike polynomial wavefront reconstruction first, we need to look at the following equation,

$$W(\rho,\theta) = Z_0 + Z_1\rho cos\theta + Z_2\rho sin\theta + Z_3(2\rho^2 - 1) + Z_4\rho^2 cos2\theta + Z_5\rho^2 sin2\theta \ldots$$

(5.3)

which can be simplify into equation

$$W(R_\rho, \theta) = \sum_{i=1}^{J} a_i F_i(\rho, \theta) \tag{5.4}$$

Following Dai's derivation(Dai, 2008), I derivate the equation with respective to x and y slope at both side of equation for the *l*th of k total sampling point, we obtain

$$\frac{\partial W(R_\rho, \theta)}{\partial x}\Big|_l = \sum_{i=1}^{J} a_i \frac{\partial F_i(\rho, \theta)}{\partial x}\Big|_l \quad (l = 1, 2, \cdots, k). \tag{5.5}$$

$$\frac{\partial W(R_\rho, \theta)}{\partial y}\Big|_l = \sum_{i=1}^{J} a_i \frac{\partial F_i(\rho, \theta)}{\partial y}\Big|_l \quad (l = 1, 2, \cdots, k). \tag{5.6}$$

so we can find the slope measurement and wavefront coefficient in the equation the matrix equation represent above value is

$$s = Ea \tag{5.7}$$

where s is the column vector of the slope measurements and a is a column vector of the unknown coefficients and the matrix

$$E = \begin{bmatrix} \frac{\partial F_1(\rho,\theta)_t}{\partial x} & \frac{\partial F_2(\rho,\theta)_1}{\partial x} & & \frac{\partial F_j(\rho,\theta)_3}{\partial x} \\ \frac{\partial F_1(\rho,\theta)_t}{\partial y} & \frac{\partial F_2(\rho,\theta)_1}{\partial y} & \cdots & \frac{\partial F_j(\rho,\theta)_3}{\partial y} \\ \vdots & & \ddots & \vdots \\ \frac{\partial F_1(\rho,\theta)_k}{\partial x} & \frac{\partial F_2(\rho,\theta)_k}{\partial x} & & \frac{\partial F_j(\rho,\theta)_k}{\partial x} \\ \frac{\partial F_1(\rho,\theta)_k}{\partial y} & \frac{\partial F_2(\rho,\theta)_k}{\partial y} & \cdots & \frac{\partial F_j(\rho,\theta)_k}{\partial y} \end{bmatrix} \tag{5.8}$$

where $\frac{\partial F_i(\rho,\theta)_t}{\partial x}$ stands for the average partial derivatives of the basis function $F_i(\rho, \theta)$ at the *l*th subaperture.

Dai (Dai, 2008) used the singular value reposition to solve the equation (5.7). Apply singular value decomposition to matrix E, we obtain matrices U and V so that E=UDV^T where D is the diagonal matrix containing the singular values of matrix E. therefore we can solve the equation to find the reconstructed wavefront through s is the slope value, *a* represent the reconstructed wavefront.

$$a = VD^{-1}U^{T}s \tag{5.9}$$

To run the Zernike Reconstruction provided in the book, I set the spacing between each hole as 1µm, and terms in the Zernike polynomial as 16. Thus, the algorithm will return the reconstruction phase 16. After that, I compare the reconstructed value with the zero gradient value, it return root means square value as 1.7813e-006.

To calculate my reconstructed wavefront and Zernike Reconstruction value difference through root mean square error algorithm, it returns 0.084.The value is small enough to show my algorithm is useful to reconstruct wavefront.
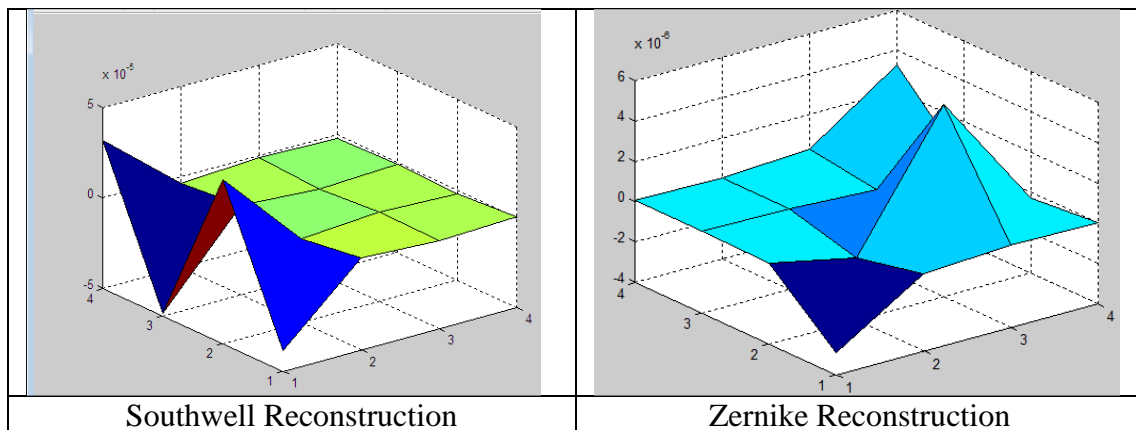

| Southwell Reconstruction | Zernike Reconstruction |

Figure 5.10 Comparisons of Southwell Wavefront Reconstruction and Zernike Wavefront Reconstruction

5.5 Gated Wavefront Sensing Simulation

Initially, I simulate a curvature wavefront by equation

$$z = \frac{x^2}{16} + \frac{y^2}{16} + 0.01 \tag{5.10}$$

After that I use a flat layer wavefront to figure the second layer surface profiling by a novel equation we proposed ourselves.
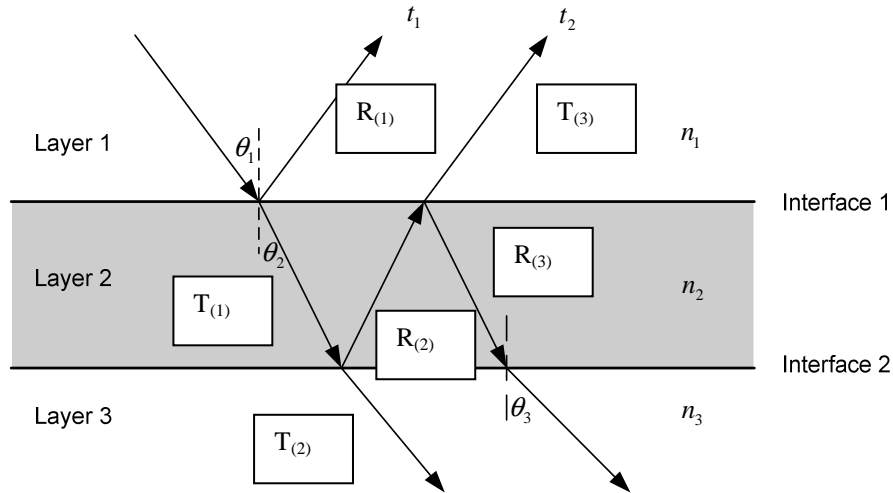
Figure 5.11 Illustration of wave propagation in multilayer

I applied Fresnel law when incident angle is 0 to help us to figure out surface profiling. In the figure 5.11, $\theta_1=0$,

$$T = \frac{4n_t n_i}{(n_t+n_i)^2} \tag{5.11}$$

$$R = \frac{(n_t-n_i)^2}{(n_t+n_i)^2} \tag{5.12}$$

1. I simulate a flat surface wavefront B=$\begin{pmatrix} 0 & 0 & 0 & 0 \\ 0 & 0 & 0 & 0 \\ 0 & 0 & 0 & 0 \\ 0 & 0 & 0 & 0 \end{pmatrix}$

2. I use it to retrieve the second layer profiling based on a proposed equation

$$F = B(i,j) + w\left(\left(\frac{T(1)\times T(2)\times T(3)}{R(1)\times R(2)\times R(3)}\times 2N\right) + \frac{C(i,j)}{A(i,j)} - B(i,j)\right)/CF \tag{5.13}$$

where w is the relaxation factor in Southwell paper

B is the flat surface wavefront

C is the output surface wavefront

A is the backprojection back input surface wavefront

N^2 is the grid number

CF =Correction factor we set it as 1000 to minimize the root means square error due to misalignment.

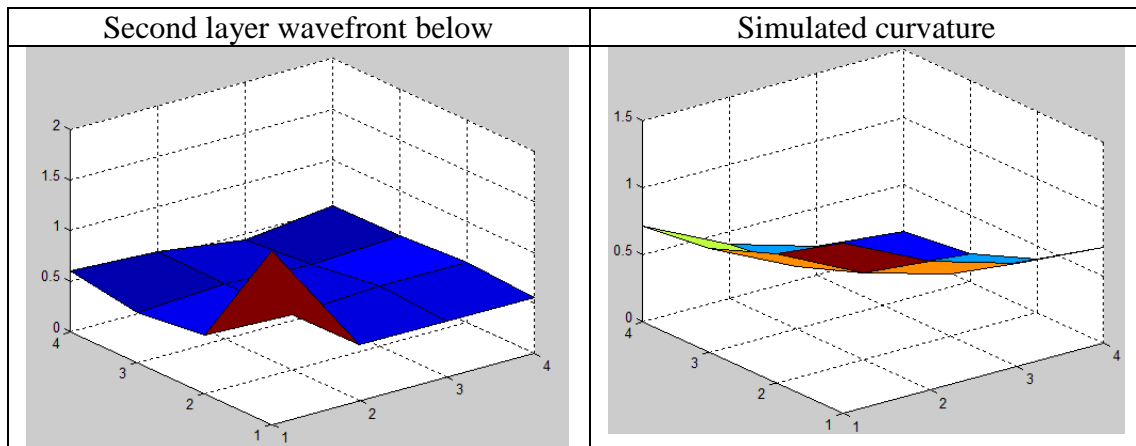Our subsurface reconstruction algorithm gives us the following result

Second layer wavefront below	Simulated curvature

Figure 5.12 Comparison of experimental wavefront and simulated wavefront

The root mean square error of this two is 0.2686

Combine the first layer surface wavefront input and output and the second layer wavefront, I achieve the wavefront in figure 5.13.
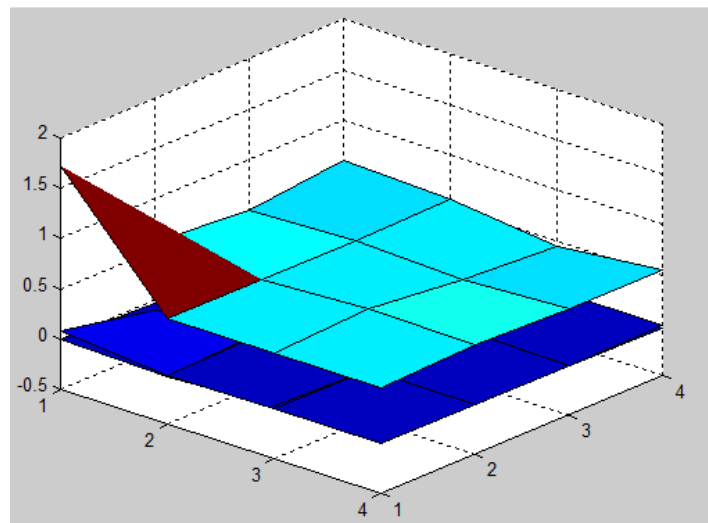

Figure 5.13 Multilayer Wavefront 3D Expression

In figure 5.13, upper surface is second layer wavefront while lower is the first layer input and output wavefront
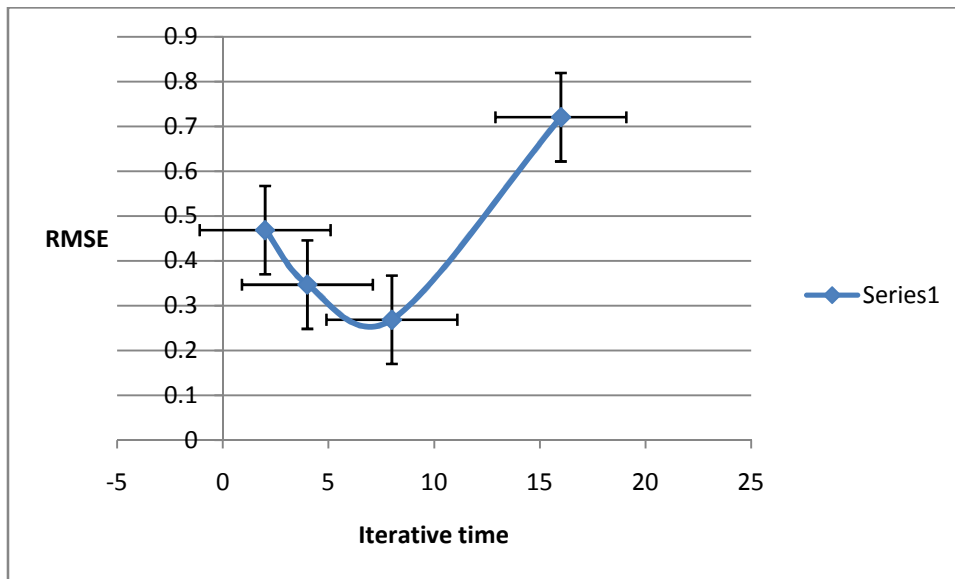
Figure 5.14 Relationships between Root Mean Square Error and Iterative Times

From figure 5.15, we can see that the root means square error is decrease following the iterative times. But after 8 iterative times, the root means square error increase. It is clear that the most suitable iterative times for running the simulation are 8.

Chapter 6

Conclusion and Recommendation

6.1 Conclusion

A low cost optical design system is built and provides results for the algorithm analysis in this project. One of limitation of the hole array is it do not provide a uniform hole shape and results in a lot of diffraction. The quality of image is poor so that it results a lot of undesirable noise in the image. Post-image processing is taken to elimination the diffraction and minimizes the noise in the image. Centroiding technique is able to detect the center of spot in this project. Wavefront phase reconstruction work well and achieve almost zero error in the project. Multilayer inspection theory shows that the Fresnel law can be applied in 3D domain and can be implemented in the real environment. It provides a way to implement the theory from graphic model to application in industry.

6.2 Recommendation

In the future, the conceptual design of the optical system can be applied on the high-tech instrument to achieve good image for research purpose. It is able to fully utilize the instrument to maximum the results' quality. The algorithm developed in this project can be used in semiconductor industry to perform defect inspection of the wafer. It offers good opportunity to cut down the cost and time for defect inspection in the industry. Multilayer inspection theory can be further developed in the industry and bring profit to the semiconductor industry.

REFERENCES

Born, M., Wolf, E., & Bhatia, A. B. (2000). *Principles of Optics: Electromagnetic Theory of Propagation, Interference and Diffraction of Light (7th edition).* CUP Archive.

Dai, G. M. (2008). Wavefront optics for vision correction. SPIE Press.

Dai, X., Hunt, M., & Schulze, M. (2003). Machine Vision Applications in Industrial Inspection XI. Proceedings of SPIE, vol. 5011. Santa Clara: CA.

Ellerbroek, B. L. (1994). Optimizing closed ioop adaptive optics performance using multiple control bandwidths. SPIE Adaptive Optics in Astronomy 2201, 935.

El-Shenawee, M. (2001). Three-Dimensional Subsurface Analysis of Electromagnetic Scattering from Penetrable/PEC Objects Buried Under Rough Surfaces: Use of the Steepest Descent Fast Multipole Method. IEEE TRANSACTIONS ON GEOSCIENCE AND REMOTE SENSING, 39(6).

Espinosa, J., Mas, D., Pérez, J., & Illueca, C. (2010). Optical surface reconstruction technique through combination of zonal and modal fitting. Journal of Biomedical Optics 15(2).

Franceschetti, G., & Riccio, D. (2008). Scattering From Layered Structures With One Rough Interface: A Unified Formulation of Perturbative Solutions. IEEE TRANSACTIONS ON GEOSCIENCE AND REMOTE SENSING, VOL. 46(NO. 6).

Germer, T. A. (2000). Polarized Light Scattering Techniques for Surface Wafer Inspection. Electronic-Enhanced Optics, Optical Sensing in Semiconductor Manufacturing, Electro-Optics in Space, Broadband Optical Networks, 2000. Digest of the LEOS Summer Topical Meetings.

Guo, H., & Wang, Z. (2006). Wavefront reconstruction using iterative discrete Fourier transformswith Fried geometry. Optik 117 77-81.

Hamamatsu, A., Shibuya, H., Oshima, Y., Maeda, S., Nishiyama, H., & Noguchi, M. (2006). STATISTICAL THRESHOLD METHOD FOR SEMICONDUCTOR INSPECTION. Paper presented at the Asia-Pacific Conference on NDT, Auckland, New Zealand.

Hartmann Wavefront Analyzer Tutorial. (2004). UTAH,USA: Spiricon, Inc.

Hecht, E. (2002). *Optics(4th edition)* . San Francisco: Addison Wesley.

Hudgin, R. H. (1977). Wave-front reconstruction for compensated imaging. J. Opt. Soc. Am. 67, 375-378.

International Technology Roadmap for Semiconductors. (2000). Semiconductor Industry Association.

Kameyama, K., & Kosugi, Y. (2002). Semiconductor Defect Classification using Hyperellipsoid Clustering Neutral Networks and Model Switching.

Kenneth Franklin Riley, M. P. H., S. J. Bence, Stephen John Bence. (2006). Mathematical methods for physics and engineering (Vol. 3rd edition): Cambridge University Press.

Levinstein, M., Rumyantsev, S., & Shur, M. (1999). Handbook Series on Semiconductor Parameters (Vol. 2). London: World Scientific.

Li, X., Zhao, L. P., Fang, Z. P., Asundi, A., & Yin, X. M. (2008). Surface measurement with Shack-Hartmann wavefront sensing technology (Proceedings Paper). Paper presented at the Ninth International Symposium on Laser Metrology.

Lin, Z. W., Zhang, X. J., & Fang, G. Y. (2009). THEORETICAL MODEL OF ELECTROMAGNETIC SCATTERING FROM 3D MULTI-LAYER DIELECTRIC MEDIA WITH SLIGHTLY ROUGH SURFACES. Progress In Electromagnetics Research , PIER 96, 37-62.

Nakamae, K., Yamaji, S., & Fujioka, H. (2000). Wafer fabrication process simulation including cost: which should be used in an inline wafer inspection strategy, high sensitivity & high cost inspection machine or low sensitivity & low cost inspection machine?

Neal, D. R. (2004). Shack-Hartmann sensor engineered for commercial measurement applications. SPIE AM100-20.

Neal, D. R., Copland, J., & Neal, D. (2002). Shack-Hartmann wavefront sensor precision and accuracy. Proceedings of SPIE Vol. 4779 (pp. 148-160). SPIE.

Neal, D. R., Pulaski, P., Raymond, T. D., & Neal, D. A. (2003). Testing highly aberrated large optics with a Shack-Hartmann wavefront sensor. SPIE 5162(19).

Poxson, D. J., Mont, F. W., Schubert, M. F., Kim, J. K., Cho, J., & Schubert, E. F. (2010). Demonstration of optical interference filters utilizing tunable refractive index layers OPTICS EXPRESS A594, 18(104).

Raymond, T., Neal, D., & Topa, D. (2002). High-speed, non-interferometric nanotopographic characterization of Si wafer surfaces. Proceedings of SPIE Vol. 4809 (pp. 208-216). SPIE.

Roopashree, M. B., Vyas, A., & Prasad, B. R. (2009). PERFORMANCE ANALYSIS OF FOURIER AND VECTOR MATRIX MULTIPLY METHODS FOR PHASE RECONSTRUCTION FROM SLOPE MEASUREMENTS. Paper presented at the ICOP 2009-International Conference on Optics and Photonics.

Schubert, M. F., Mont, F. W., Chhajed, S., Poxson, D. J., Kim, J. K., & Schubert, E. F. (2008). Design of multilayer antireflection coatings made from co-sputtered and low refractive-index materials by genetic algorithm OPTICS EXPRESS 5290, 16(8).

Schulze, M. A., Hunt, M. A., Voelkl, E., Hickson, J. D., & Usry, W. (2003). Semiconductor wafer defect detection using digital holography. Process and Materials Characterization and Diagnostics in IC Manufacturing II. Society of Photo-Optical Instrumentation Engineers.
.
Shankar, N., & Zhong, Z. (2004). Defect detection on semiconductor wafer surfaces. Microelectronic Engineering 77, 337–346.

Sluzek, A., & Tan, C. (2004). Visual detection of 3D Obstacles Using Gated Images. 8th International Conferences on Control Automation, Robotics and Vision. Kunming,China.

Southwell, W. H. (1980). Wave-front estimation from wave-front slope measurements. J. Opt. Soc. Am., Vol. 70, No. 8, p998-1006.

Stokowski, S., & Vaez-iravani, M. (1999). Wafer Inspection Technology Challenges for ULSI Manufacturing.

Tyson, R. K. (2000). Adaptive optics engineering handbook. New York : CRC Press.

Udupa, G., Ngoi, B. K., Goh, H. C., & Yusoff, M. N. (2004). Defect detection in unpolished Si wafers by digital shearography. Measurement Science and Technology.

Vyas, M. B. Roopashree, & B.R.Prasad. (2010). Centroid Detection by Gaussian Pattern Matching In Adaptive Optics. International Journal of Computer Applications (0975 - 8887), Volume 1 – No.26.

Woo, S. Y., Ueda, T., Ishigaki, T., & Kang, K. (2010). Optical Characterization of Surface Profile of Various Si1-xGex/Si Wafers.

WU, W. W., SUN, H. Y., & SONG, F. H. (2009). A New Wavefront Reconstruction mehtod based on simulate H-S sensor. Journal of the Academy of Equipment Command＆Technology, 20(5).

Yin, X., Li, X., Zhao, L., & Fang, Z. (2009). Automatic Centroid Detection for Shack-Hartmann Wavefront Sensor. Paper presented at the 2009 IEEE/ASME International Conference on Advanced Intelligent Mechatronics, Suntec Convention and Exhibition Center Singapore.